CMS Physics Analysis Summary

Contact: cms-pag-conveners-susy@cern.ch 2018/09/08

Inclusive search for supersymmetry using razor variables in pp collisions at $\sqrt{s} = 13$ TeV

The CMS Collaboration

Abstract

An inclusive search for supersymmetry with the razor variables is performed using a data sample of proton-proton collisions corresponding to an integrated luminosity of 35.9 fb^{-1} collected with the CMS experiment in 2016 at a center-of-mass energy of $\sqrt{s} = 13$ TeV. The search covers final states with zero or one charged lepton and features event categories divided according to the presence of a high-transverse momentum hadronically decaying W boson or top quark, the number of jets, the number of b-tagged jets, and the values of the razor kinematic variables in order to separate signal from background for a wide variety of supersymmetric particle signatures. The combination of the zero-lepton, one-lepton, and boosted W boson and top quark event categories increases the sensitivity particularly to signal models with large mass splitting between the produced gluino or squark and the lightest supersymmetric particle. Limits on the gluino mass extend to 2.0 TeV while limits on top squark masses reach 1.14 TeV.

1 Introduction

We present an inclusive search for supersymmetry (SUSY) using the razor variables [1, 2] on data collected by the CMS detector in 2016. SUSY extends space-time symmetry such that every fermion (boson) in the standard model (SM) has a bosonic (fermionic) partner [3–11]. Supersymmetric extensions of the SM yield solutions to the gauge hierarchy problem without the need for large fine tuning of fundamental parameters [12–17], exhibit gauge coupling unification [18–23], and can provide weakly interacting particle candidates for dark matter [24, 25].

The search described in this note is a direct extension of the previous work in [1] and [2]. The search is inclusive in scope, covering final states with zero or one lepton. To enhance sensitivity to specific types of SUSY signatures, the events are categorized according to the presence of jets consistent with high-transverse momentum hadronically decaying W bosons or top quarks, the number of leptons, jets, and b-tagged jets identified and the search is performed in bins of the razor variables M_R and R^2. The result presented here is the first search for SUSY from the CMS experiment that incorporates both boosted and non-boosted event categories. This search strategy provides broad sensitivity to gluino and squark pair production in R-parity conserving scenarios for a large variety of decay modes and branching ratios. The prediction of the standard model (SM) background in the search regions is performed using Monte Carlo simulation calibrated using data control regions that isolate the major background components. Additional validation of the assumptions made by the background estimation method yield estimates of the systematic uncertainties.

Other searches for SUSY by the CMS [26–33] and ATLAS [34–40] Collaborations have been performed using similar datasets and yield complementary sensitivity. The analysis presented in this note extends the sensitivity of previous searches by combining the one-lepton and zero-lepton final states. Furthermore, alternative kinematic variables, such as the razor variables presented in this study enhance the global sensitivity to new physics by expanding the phase space regions in which we search, and by adding robustness in the understanding of the composition and potential systematic errors of the background model. To give a characteristic example, for squark pair production with squark mass of 1000 GeV and neutralino mass of 100 GeV, we find that 30–50% of signal events falling in the most sensitive tail regions of the razor kinematic variables do not fall in the most sensitive regions of kinematic variables used in alternative analyses.

We present interpretations of the results in terms of production cross section limits on several simplified models for which this search has enhanced sensitivity. The simplified models considered include gluino-pair production decaying to a pair of top quarks and the lightest supersymmetric particle (LSP) referred to as "T1tttt", gluino pair-production decaying to a top quark and a low mass top squark, which subsequently decays to a charm quark and the LSP referred to as "T5ttcc", and top squark pair production referred to as "T2tt".

The remainder of this note is organized as follows. Details of the detector, trigger, and object reconstruction and identification are described in Section 2. The Monte Carlo simulation samples used to model background and signal processes are described in Section 3. The analysis strategy and event categorization are discussed in Section 4, and the background modeling is discussed in Section 5. Systematic uncertainties are discussed in Section 6, and finally the results and interpretations are presented in Section 7.

2 CMS Detector and Object Reconstruction

The CMS detector consists of a superconducting solenoid of 6 m internal diameter, providing a magnetic field of 3.8 T. Within the superconducting solenoid volume are a silicon pixel and a silicon strip tracker, a lead-tungstate crystal electromagnetic calorimeter, and a brass/scintillator hadron calorimeter, each composed of a barrel and two endcap sections. Muons are measured in gas-ionization detectors embedded in the magnet steel flux-return yoke outside the solenoid. Extensive forward calorimetry complements the coverage provided by the barrel and endcap detectors. Events are selected by a two-level trigger system. The first level (L1) is based on a hardware filter, and the second level, the high level trigger (HLT) is implemented in software. A more detailed description of the CMS detector, together with a definition of the coordinate system used and the relevant kinematic variables, can be found in Ref. [41].

Physics objects are defined using the particle-flow (PF) algorithm [42], which reconstructs and identifies each individual particle using an optimized combination of information from the various elements of the CMS detector. All PF objects are clustered into jets using the anti-k_{T} algorithm [43, 44] with a size parameter of 0.4. Jet energy corrections are derived from simulation and confirmed by in-situ measurements of the energy balance in dijet and photon+jet events. To identify jets originating from bjets, we use the "medium" working point of the combined secondary vertex (CSV) b-jet tagger, which uses an inclusive vertex finder to select bjets [45]. The efficiency to identify a bjet is in the range of 50–65% for jets with p_{T} between 20 and 400 GeV, while the misidentification rate for light-flavor and gluon jets (charm jets) is about $1\%(10\%)$. We also use the "loose" working point of the CSV b-jet tagger, which has an efficiency of 80% and a misidentification rate of 10% to identify bjets to be vetoed while defining various control regions.

Wide jets used for identifying boosted W bosons and top quarks are clustered using the anti-k_{T} algorithm with a size parameter of 0.8. Identification is done using jet mass, the N-subjettiness variables [46], and subjet b-tagging for top quarks. Jet mass is computed using the soft drop algorithm [47]. The N-subjettiness variables

$$\tau_N = \frac{1}{d_0} \sum_k p_{\mathrm{T},k} \min\left(\Delta R_{1,k}, \Delta R_{2,k}, \cdots, \Delta R_{N,k}\right), \tag{1}$$

where N denotes candidate axes for subjets, k runs over all constituent particles, and $d_0 = R_0 \sum_k p_{\mathrm{T},k}$, evaluate the consistency of a jet with having N subjets. To enhance discrimination, the ratios $\tau_{21} = \tau_2/\tau_1$ and $\tau_{32} = \tau_3/\tau_2$ are used for W boson and top quark tagging respectively. For tagging top quarks, an additional requirement on subjet b-tagging based on the multivariate CSV algorithm is imposed [45].

The missing transverse momentum vector $\vec{p}_{\mathrm{T}}^{\,\mathrm{miss}}$ is defined as the projection of the negative vector sum of the momenta of all reconstructed PF particles on the plane perpendicular to the beams. Its magnitude is referred to as $p_{\mathrm{T}}^{\mathrm{miss}}$. Electrons are reconstructed by associating an energy cluster in the ECAL with a reconstructed track [48], and are identified on the basis of the electromagnetic shower shape, the ratio of energy deposited in the electromagnetic and hadronic calorimeters, the geometric matching of the track to the calorimeter cluster, the track quality and impact parameter, and isolation. Muons are reconstructed by combining tracks found in the muon system with corresponding tracks in the silicon tracking detectors [49], and are identified based on the quality of the track fit, the number of detector hits used in the tracking algorithm, the compatibility between track segments, and isolation. Two types of selections are defined for electrons and muons: a "tight" selection with an average efficiency of about 70–75% and a "veto" selection with an efficiency of about 90–95%. Hadronically decaying tau lep-

tons are reconstructed using the hadron-plus-strips algorithm [50], which identifies tau decay modes with one charged hadron and up to two neutral pions or three charged hadrons, and are required to be isolated. The "loose" selection is used and results in an efficiency of about 50% for successfully reconstructed τ_h decays. Finally, photon candidates are reconstructed from energy clusters in the ECAL [51] and identified based on the transverse shower width, the hadronic to electromagnetic energy ratio (H/E) in the HCAL and ECAL, and isolation. Photon candidates that share the same energy cluster as an identified electron are vetoed.

3 Simulation

Monte Carlo simulation samples (from here on referred to as MC) are used to predict the SM backgrounds in the search regions and to calculate the selection efficiencies for SUSY signal models. Events corresponding to the Z+jets, γ+jets, and QCD multijet background processes, as well as the SUSY signal processes, are generated with MADGRAPH V5 [52] interfaced with PYTHIA V8.2 [53, 54] for fragmentation and parton showering, and matched to the matrix element kinematic configuration using the MLM algorithm [55, 56]. Other background processes are generated with MADGRAPH_aMC@NLO 2.2 [57] (W+jets, s-channel single top, $t\bar{t}W$, $t\bar{t}Z$) and with POWHEG v2 [58–60] ($t\bar{t}$+jets, t-channel single top, and tW), both interfaced with PYTHIA V8.2. SM background events are simulated using a GEANT4-based model [61] of the CMS detector, while SUSY signal events are simulated using the CMS fast simulation package [62].

The SUSY particle production cross sections are calculated to next-to-leading order (NLO) plus next-to-leading-logarithm (NLL) accuracy [63–68], assuming all SUSY particles other than those in the relevant diagrams to be too heavy to participate in the interaction. The NLO+NLL cross sections and their associated uncertainties [69] are taken as a reference to derive the exclusion limit on the SUSY particle masses.

To improve on the MadGraph modeling of the multiplicity of additional jets from initial state radiation (ISR), Madgraph-generated $t\bar{t}$ SUSY signal are re-weighted based on the number of ISR jets (N_J^{ISR}) so as to make the jet multiplicity agree with data. The re-weighting factors vary between 0.92 and 0.51 for N_J^{ISR} between 1 and 6. We take one half of the deviation from unity as the systematic uncertainty in these re-weighting factors.

4 Analysis Strategy and Event Categorization

We perform the search in several event categories defined according to the presence of jets tagged as boosted hadronic W boson or top quark decays, the number of identified charged leptons, jets, and b-tagged jets. Events in the one-lepton category are required to have one and only one charged lepton (electron or muon) with p_T above 25 GeV for muons and 30 GeV for electrons selected using the tight criteria, while events in the zero-lepton category are required to have no electrons or muons passing the tight or veto selection criteria and no hadronic taus.

Zero-lepton events with jets tagged as originating from a boosted hadronic W boson or top quark decay are placed in a dedicated "boosted" event category. Events in this "boosted" category are analyzed separately with a set of control regions and closure tests specific for final states with boosted objects. They are are further classified into those having at least one tagged W boson and one tagged b quark ("W" category), and those having at least one tagged top quark ("Top" category). Events in the "W" category are further divided according to jet multiplicity, into subcategories with 4–5 jets ("Wnj45" category), and 6 jets and more ("Wnj6" category).

Events not tagged as having boosted W bosons or top quarks are placed into named categories according to the number of selected jets and charged leptons. One-lepton events are placed in the "Lepton Seven-jet" category if they have 7 or more selected jets, and placed in the "Lepton Multijet" category if they have between 4 and 6 jets. One-lepton events with fewer than 4 jets are not considered in the analysis. Events with zero leptons are placed in the "Seven-jet" category if they have 7 or more selected jets, the "Multijet" category if they have between 4 and 6 jets, and the "Dijet" category if they have two or three jets. The Dijet category is further divided into subcategories with zero, one, and two or more b-tagged jets, and all other categories are divided into subcategories with zero, one, two, and three or more b-tagged jets. The full set of search categories and their requirements are summarized in Table 1.

For each event in the above categories, we group the selected charged leptons and jets in the event into two distinct hemispheres called megajets whose four-momenta are defined as the vector sum of the four-momenta of the physics objects in each hemisphere. The clustering algorithm selects the grouping that minimizes the sum of the squares of the invariant masses of the two megajets [70]. We define the razor variables M_{R} and $M_{\mathrm{T}}^{\mathrm{R}}$ as:

$$M_{\mathrm{R}} \equiv \sqrt{(|\vec{p}^{\,\mathrm{j}_1}| + |\vec{p}^{\,\mathrm{j}_2}|)^2 - (p_{\mathrm{z}}^{\mathrm{j}_1} + p_{\mathrm{z}}^{\mathrm{j}_2})^2}, \tag{2}$$

$$M_{\mathrm{T}}^{\mathrm{R}} \equiv \sqrt{\frac{p_{\mathrm{T}}^{\mathrm{miss}}(p_{\mathrm{T}}^{\mathrm{j}_1} + p_{\mathrm{T}}^{\mathrm{j}_2}) - \vec{p}_{\mathrm{T}}^{\,\mathrm{miss}} \cdot (\vec{p}_{\mathrm{T}}^{\,\mathrm{j}_1} + \vec{p}_{\mathrm{T}}^{\,\mathrm{j}_2})}{2}}, \tag{3}$$

where $\vec{p}_{\mathrm{j}_i}$, $\vec{p}_{\mathrm{T}}^{\,\mathrm{j}_i}$, and $p_{\mathrm{z}}^{\mathrm{j}_i}$ are the momentum of the i'th megajet, its transverse component with respect to the beam axis, and its longitudinal component, respectively. The dimensionless variable R is defined as:

$$\mathrm{R} \equiv \frac{M_{\mathrm{T}}^{\mathrm{R}}}{M_{\mathrm{R}}}. \tag{4}$$

Single electron or muon triggers are used to collect events in the one-lepton categories, with a trigger efficiency of about 80% for p_{T} around 30 GeV, growing to 95% for p_{T} above 50 GeV. Events in the boosted category are collected using triggers that select based on the p_{T} of the leading jet and the scalar sum H_{T} of the transverse momentum of all jets. The trigger efficiency is about 50% at the low range of the M_{R} and R^2 kinematic variables and grows to 100% for $M_{\mathrm{R}} > 1.2$ TeV and $\mathrm{R}^2 > 0.16$. For the zero-lepton nonboosted event categories, dedicated triggers requiring at least two jets and loose thresholds on the razor variables M_{R} and R^2 are used to collect the events. The trigger efficiency ranges from 95 to 100% and increases with M_{R} and R^2.

Pre-selection requirements on the M_{R} and R^2 variables are made depending on the event category. For events in the one-lepton categories, further requirements are made on the transverse mass M_{T} computed using the charged lepton momentum and the $\vec{p}_{\mathrm{T}}^{\,\mathrm{miss}}$. For events in the zero-lepton categories, further requirements are made on the azimuthal angle $\Delta\phi_{\mathrm{R}}$ between the axes of the two razor megajets. These requirements are summarized in Table 2.

Events containing signatures consistent with beam-induced background or anomalous noise in the calorimeters are rejected using dedicated filters [71, 72]. Finally, in each event category, the search is performed in bins of the kinematic variables M_{R} and R^2 in order to take advantage of the varying signal-to-background ratio in the different bins. For one-lepton categories, the search regions are composed of five bins in M_{R}, starting from 550 GeV, and five bins in R^2 starting from 0.20. For the zero-lepton boosted categories, the search regions are composed

Table 1: Summary of the search categories, their charged lepton and jet count requirements, and the b-tag bins that define the subcategories. Events passing the "Lepton Veto" requirement must have no tight electron or muon, no veto electron or muon, and no hadronic taus.

Category	Lepton Requirement	Jet Requirement	b-tag Bins
Lepton Multijet	1 "Tight" electron or muon	4–6 jets	0, 1, 2, $\geq$ 3 b-tags
Lepton Seven-jet	1 "Tight" electron or muon	$\geq$ 7 jets	0, 1, 2, $\geq$ 3 b-tags
Boosted Wnj45	Lepton Veto	$\geq$ 1 W tagged jet 4–5 jets	$\geq$ 1 b-tags
Boosted Wnj6	Lepton Veto	$\geq$ 1 W tagged jet $\geq$ 6 jets	$\geq$ 1 b-tags
Boosted Top	Lepton Veto	0 W tagged jets $\geq$ 1 top tagged jet $\geq$ 6 jets	$\geq$ 0 b-tags
Dijet	Lepton Veto	0 W tagged jets 0 top tagged jets 2–3 jets	0, 1, $\geq$ 2 b-tags
Multijet	Lepton Veto	0 W tagged jets 0 top tagged jets 4–6 jets	0, 1, 2, $\geq$ 3 b-tags
Seven-jet	Lepton Veto	0 W tagged jets 0 top tagged jets $\geq$ 7 jets	0, 1, 2, $\geq$ 3 b-tags

Table 2: The baseline requirements on the razor variables M_R and R^2, additional requirements on M_T and $\Delta\phi_R$, and the trigger requirements are shown for each event category.

Category	Pre-selection	Additional Requirements	Trigger Requirement
Lepton Multijet	$M_R > 550$ & $R^2 > 0.20$	$M_T > 120$ GeV	Single Lepton
Lepton Seven-jet	$M_R > 550$ & $R^2 > 0.20$	$M_T > 120$ GeV	Single Lepton
Boosted Wnj45	$M_R > 800$ & $R^2 > 0.08$	$\Delta\phi_R < 2.8$	H_T, jet p_T
Boosted Wnj6	$M_R > 800$ & $R^2 > 0.08$	$\Delta\phi_R < 2.8$	H_T, jet p_T
Boosted Top	$M_R > 800$ & $R^2 > 0.08$	$\Delta\phi_R < 2.8$	H_T, jet p_T
Dijet	$M_R > 650$ & $R^2 > 0.30$	$\Delta\phi_R < 2.8$	Hadronic Razor
Multijet	$M_R > 650$ & $R^2 > 0.30$	$\Delta\phi_R < 2.8$	Hadronic Razor
Seven-jet	$M_R > 650$ & $R^2 > 0.30$	$\Delta\phi_R < 2.8$	Hadronic Razor

of five bins in M_R, starting from 800 GeV, and five bins in R^2, starting from 0.08. Finally, for the zero-lepton nonboosted categories, the search regions are composed of five bins in M_R, starting from 650 GeV, and four bins in R^2 starting from 0.30. In each category, to avoid too many unpopulated bins, they are merged such that the expected background in each bin is larger than about 0.1 events. As a result, the search regions have a decreasing number of bins as the number of jets, b-tagged jets, and M_R increases.

5 Background Modeling

The main background processes in the search regions considered are W($\ell\nu$)+jets (with ℓ = e, μ, τ), Z($\nu\bar{\nu}$)+jets, $\mathrm{t\bar{t}}$, and QCD multijet production. For event categories with zero b-tagged jets, the background is primarily composed of the W($\ell\nu$)+jets and Z($\nu\bar{\nu}$)+jets processes, while for categories with two or more b-tagged jets it is dominated by the $\mathrm{t\bar{t}}$ process. There are also small contributions from single top quark production, production of two or three electroweak bosons, and production of $t\bar{t}$ in association with a W or Z.

The background prediction strategy relies on the use of control regions to isolate each background process, address any deficiencies of the MC simulation in a data driven way, and estimate systematic uncertainties in the expected event yields. For the dominant backgrounds discussed above, the primary sources of mismodeling come from inaccuracy in the MC prediction of the hadronic recoil spectrum and the jet multiplicity. Corrections to the MC simulation are applied in bins of M_R, R^2, and the number of jets (N_jets) to address these modeling inaccuracies. The control region bins generally follow the bins of the search regions described in Section 4, but bins with limited statistical power are merged in order to avoid large random statistical fluctuations in the background predictions.

For the boosted categories, slightly different control region selection and categorization are used and discussed in Section 5.4. An additional validation of the background prediction method is also performed for the boosted categories.

In what follows, all background MC samples are corrected for known mismodeling of the jet energy response, the trigger efficiency, and the selection efficiency of electrons, muons, and b-tagged jets. These corrections are mostly in the range of 0–5%, but can be as large as 10% in extreme cases.

5.1 $\mathrm{t\bar{t}}$ and W($\ell\nu$)+jets Background

Corrections to the hadronic recoil in the $\mathrm{t\bar{t}}$ and W($\ell\nu$)+jets MC are derived in a control region consisting of events having at least one tight muon or electron. Kinematic cuts are applied in order to separate the control region from the analysis search region and to reduce the QCD multijet background. The $p_\mathrm{T}^\mathrm{miss}$ is required to be larger than 30 GeV, and M_T is required to be between 30 and 100 GeV.

The one-lepton control sample is separated into W($\ell\nu$)+jets enriched and $\mathrm{t\bar{t}}$ enriched samples by requiring events have zero (for W($\ell\nu$)+jets), or one or more (for $\mathrm{t\bar{t}}$) b-tagged jets, respectively. The purity of the W($\ell\nu$)+jets and $\mathrm{t\bar{t}}$ dominated control regions are both about 80%. In each sample, corrections to the MC prediction are derived in two-dimensional bins in M_R and R^2. The contribution from all other background processes estimated from MC in each bin in a given control region ($N_{\text{CR bin i}}^{\text{MC,bkg}}$) is subtracted from the data yield in the corresponding bin in the control region ($N_{\text{CR bin i}}^{\text{data}}$), and compared to the MC prediction ($N_{\text{CR bin i}}^{\text{MC,}\mathrm{t\bar{t}}}$) to derive the correction factor :

$$C_{\text{bin i}}^{\mathrm{t\bar{t}}} = \frac{N_{\text{CR bin i}}^{\text{data}} - N_{\text{CR bin i}}^{\text{MC,bkg}}}{N_{\text{CR bin i}}^{\text{MC,}\mathrm{t\bar{t}}}}. \tag{5}$$

Because the $\mathrm{t\bar{t}}$ enriched sample is the purer of the two, the corrections are derived in this sample first. These corrections are applied to the $\mathrm{t\bar{t}}$ MC in the W($\ell\nu$)+jets enriched sample, and then analogous corrections to the W($\ell\nu$)+jets MC are derived. The distribution in bins of M_R and R^2 in the $\mathrm{t\bar{t}}$ control region is shown in Figure 1.

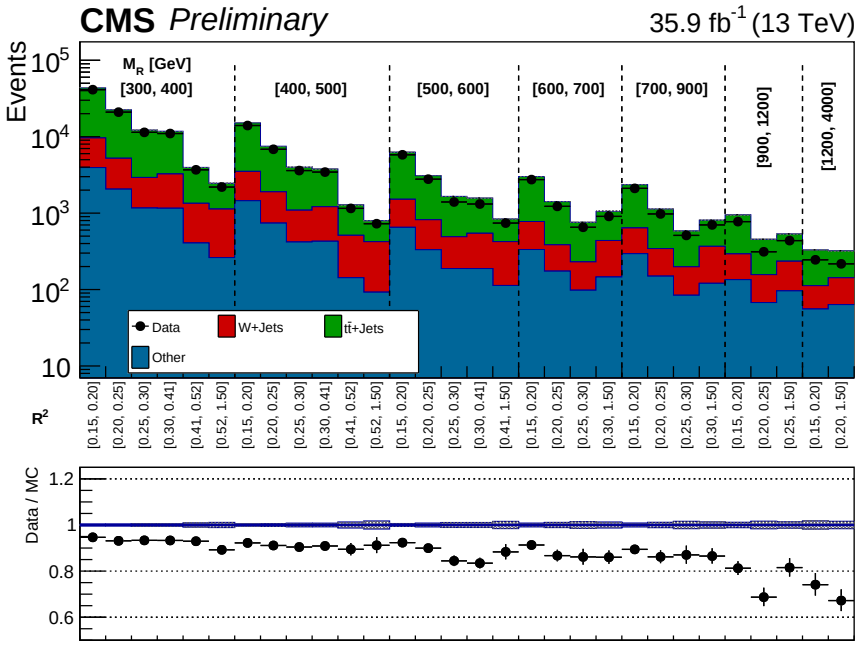

Figure 1: The M_R-R^2 distribution observed in data is shown along with the MC prediction in the $t\bar{t}$ one-lepton control region. The two-dimensional M_R-R^2 distribution is shown in a one dimensional representation, with each M_R bin marked by the dashed lines and labeled near the top, and each R^2 bin labeled below. The ratio of data to the MC simulation prediction is shown on the bottom inset, with the statistical uncertainty expressed through the data point error bars and the systematic uncertainty of the background prediction represented by the shaded region. The corrections derived from background control regions have not been applied yet.

The corrections based on M_R and R^2 are measured and applied inclusively in the number of selected jets. As our search regions are divided according to jet multiplicity, additional corrections are needed in order to ensure correct background modeling for different numbers of jets. We derive these corrections separately for the $t\bar{t}$ and $W(\ell\nu)$+jets samples, obtaining correction factors for events with two or three jets, four to six jets, and seven or more jets. The $t\bar{t}$ correction is derived prior to the $W(\ell\nu)$+jets correction to take advantage of the slightly higher purity of the $t\bar{t}$ control region.

We also check for MC mismodeling that depends on the number of b-jets in the event. To do this we apply the above-mentioned corrections in bins of M_R, R^2, and the number of jets and derive an additional correction needed to make the predicted M_R spectrum match that in data for each b-tag multiplicity. This correction is performed separately for events with two or three, four to six, and seven or more jets.

A final validation of the MC modeling in this one-lepton control region is completed by comparing the R^2 spectrum in data with the MC prediction in each jet multiplicity and b-tag multiplicity category. We do not observe any systematic mismodeling in the R^2 spectra, and we propagate the total uncertainty in the data-to-MC ratio in each bin of R^2 as a systematic uncertainty in the $t\bar{t}$ and W+jets backgrounds in the analysis search regions.

The $t\bar{t}$ background in the one-lepton control region is composed mostly of lepton+jets $t\bar{t}$ events, where one top quark decayed fully hadronically and the other top quark decayed leptonically. In the leptonic analysis search regions, the M_T cut suppresses lepton+jets $t\bar{t}$ events, and the dominant remaining $t\bar{t}$ background consists of $t\bar{t}$ events where both top quarks de-

cayed leptonically, and one of the two leptons is not identified. It is therefore important to validate that the corrections to the $t\bar{t}$ MC derived in the one-lepton control region also describe dileptonic $t\bar{t}$ events well. We perform this check by selecting an event sample enriched in dileptonic $t\bar{t}$ events, applying the corrections on the $t\bar{t}$ MC prediction derived in the one-lepton control region, and evaluating the consistency of the data with the corrected prediction. This check is performed separately for each jet multiplicity category used in the analysis search regions. The dilepton $t\bar{t}$ enriched sample consists of events with two tight electrons or muons with $p_T > 30\,\text{GeV}$ and invariant mass larger than 20 GeV, at least one b-tagged jet, and $p_T^{\text{miss}} > 40\,\text{GeV}$. Events with two same-flavor leptons with invariant mass near the Z boson mass are rejected to suppress Drell-Yan background. The M_T cut is applied to one of the leptons in each event, and the other is treated as though it were not identified. A systematic uncertainty in the dilepton $t\bar{t}$ background is assessed by comparing data with MC prediction in the M_R distribution for each jet multiplicity category. The M_R distributions in the $t\bar{t}$ dilepton control region for the two to three and four to six jet event categories are displayed in Figure 2.

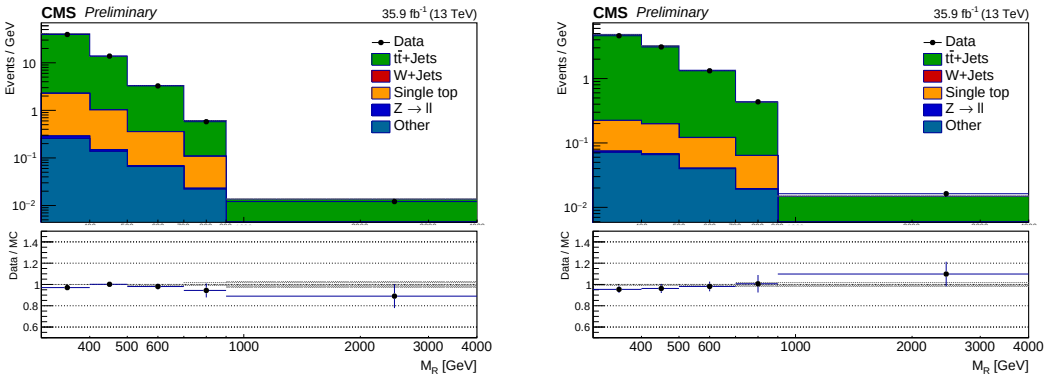

Figure 2: The M_R distribution in the $t\bar{t}$ dilepton control region is displayed in the 2–3 and 4–6 jet categories along with the corresponding MC predictions. The corrections derived from the $t\bar{t}$ and W+jets control regions have been applied.

The MC prediction for the hadronic search regions can be affected by potential mismodeling of the veto identification efficiency for muons, electrons, and taus. Two control samples, the veto lepton and veto hadronic tau samples, are defined in order to assess the modeling of this efficiency in MC. Events in the veto lepton (veto hadronic tau) sample are required to have at least one veto lepton (hadronic tau) and pass one of the hadronic razor triggers. These events must also have M_T between 30 GeV and 100 GeV, $M_R > 400\,\text{GeV}$, $R^2 > 0.25$, and at least two jets with $p_T > 80\,\text{GeV}$. The data and MC prediction are compared in bins of lepton p_T and η for each jet multiplicity category. A systematic uncertainty is assigned to cover to cover the difference between data and prediction in the lepton p_T spectrum. No further systematic mismodeling is observed in the lepton η distributions, and the size of the uncertainty in each η bin is propagated as an uncertainty in the analysis search region predictions. The lepton p_T distributions obtained in the veto lepton control region for the categories with two to three and four to six jets are displayed in Figure 3.

5.2 $Z \to \nu\bar{\nu}$ Background

To predict the background contribution from the $Z(\nu\bar{\nu})$+jets process, we take advantage of its kinematic similarity with the $Z \to \ell\ell$, $W(\ell\nu)$+jets, and γ+jets processes. Corrections to the hadronic recoil and jet multiplicity spectra are obtained in a control sample enriched in γ+jets events, and the validity of these corrections is checked in a second control sample enriched in $W(\ell\nu)$+jets events. A third control sample, enriched in $Z \to \ell\ell$ events, is used to normal-

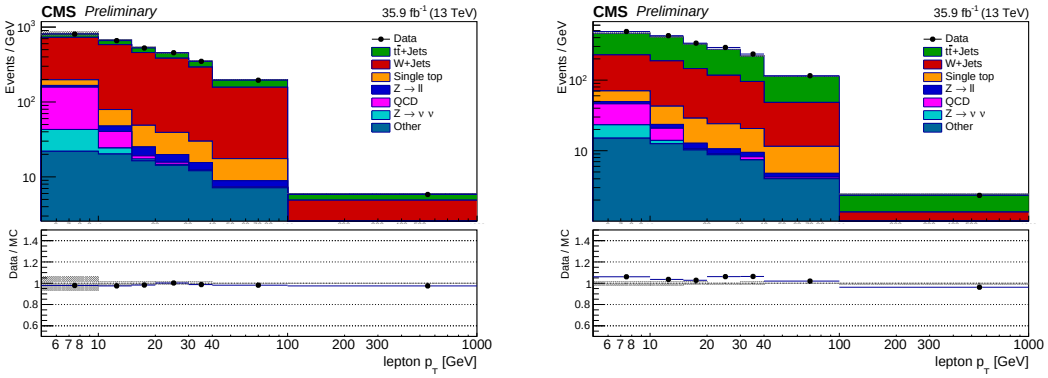

Figure 3: The p_{T} distribution for leptons passing the veto identification criteria is displayed in the 2–3 and 4–6 jet categories along with the corresponding MC predictions. The corrections derived from the $\mathrm{t\bar{t}}$ and W+jets control regions have been applied.

ize the obtained correction factors and to provide an additional consistency check of the MC prediction.

The γ+jets control sample consists of events having at least one selected photon and passing a set of kinematic requirements. Photons are required to have $p_{\mathrm{T}} > 185\,\mathrm{GeV}$ and pass loose identification and isolation criteria. The photon is treated as invisible – its transverse momentum is added vectorially to the $\vec{p}_{\mathrm{T}}^{\,\mathrm{miss}}$, and it is ignored in the calculation of M_{R} – in order to simulate the invisible Z decay products in a $\mathrm{Z} \to \nu\bar{\nu}$+jets event. Selected events must pass a single photon trigger, have two jets with $p_{\mathrm{T}} > 80\,\mathrm{GeV}$, and have $M_{\mathrm{R}} > 400\,\mathrm{GeV}$ and $\mathrm{R}^2 > 0.25$.

The contribution of misidentified photons to the yield in this control sample is estimated via a template fit to the distribution of the photon charged isolation. The fit is performed in bins of M_{R} and R^2 and yields an estimate of the purity of the photon sample in each bin. Contributions from other background processes such as $\mathrm{t\bar{t}}\gamma$ are estimated using MC. Additionally, events in which the photon is produced within a jet are considered to be background. Corrections to the hadronic recoil in MC are derived in this control region by subtracting the estimated background yields from the number of observed counts, and comparing the resulting yield with the prediction from the γ+jets MC, in each bin of M_{R} and R^2. The two-dimensional distribution of M_{R} and R^2 in the photon control region is displayed in Fig. 4.

As in the one-lepton control region described in Section 5.1, an additional correction is derived to account for possible MC mismodeling as a function of the jet multiplicity. This correction is derived for events with two or three jets, with four to six jets, and with seven or more jets. After these corrections are applied, the data in the control region is compared with the MC prediction in bins of the number of b-tagged jets. As in the one-lepton control region, the M_{R} spectra in MC are corrected to match the data in each b-tag category, and a systematic uncertainty in the $\mathrm{Z}(\nu\bar{\nu})$+jets background is assigned based on the size of the uncertainty in each bin of R^2.

A check of the $\mathrm{Z}(\nu\bar{\nu})$+jets prediction is performed on a sample enriched in $\mathrm{Z} \to \ell^+\ell^-$ decays. Events in this sample are required to have two tight electrons or two tight muons having an invariant mass consistent with the Z mass. The two leptons are treated as invisible for the purpose of computing the razor variables. Events must have no b-tagged jets, two or more jets with $p_{\mathrm{T}} > 80\,\mathrm{GeV}$, $M_{\mathrm{R}} > 400\,\mathrm{GeV}$, and $\mathrm{R}^2 > 0.25$. The correction factors obtained from the γ+jets control region are normalized so that the total MC prediction in the $\mathrm{Z} \to \ell^+\ell^-$+jets control region matches the observed data yield. This corrects for the difference between the true γ+jets cross section and the leading-order cross section used to normalize the MC. Small residual disagreements between data and MC in the M_{R} and R^2 distributions are propagated

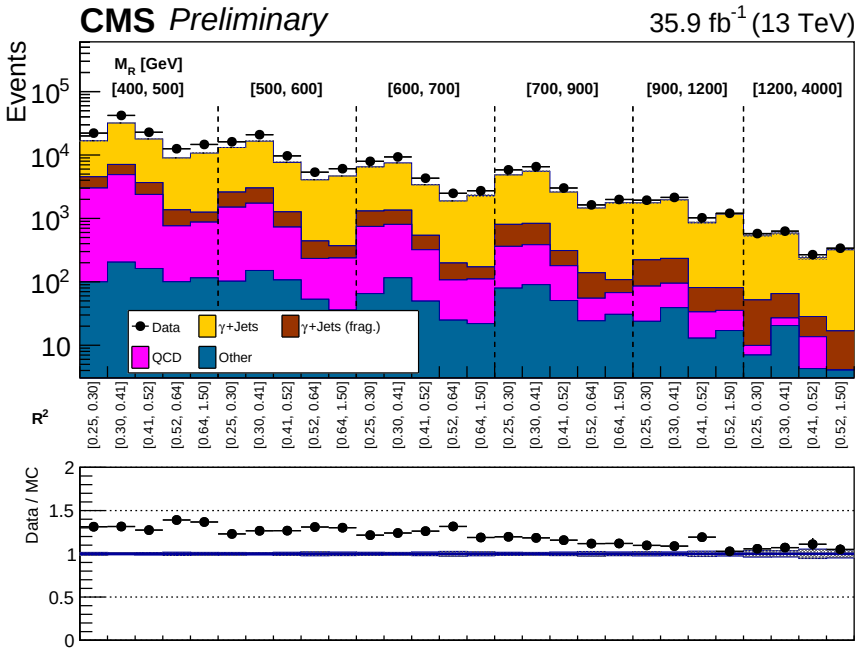

Figure 4: The M_R-R^2 distribution observed in data is shown along with the MC prediction in the photon+jets control region. The two-dimensional M_R-R^2 distribution is shown in a one dimensional representation, with each M_R bin marked by the dashed lines and labeled near the top, and each R^2 bin labeled below. The ratio of data to the background prediction is shown on the bottom inset, with the statistical uncertainty expressed through the data point error bars and the systematic uncertainty of the background prediction represented by the shaded region. The contribution from the γ+jets process where the photon was produced from a jet fragmentation is labeled as "γ+jets (frag.)". The corrections derived from background control regions have not been applied yet in this figure.

as systematic uncertainties in the $Z(\nu\bar{\nu})$+jets prediction. The M_R distributions in this control region for the two to three and four to six jet categories are shown in Figure 5.

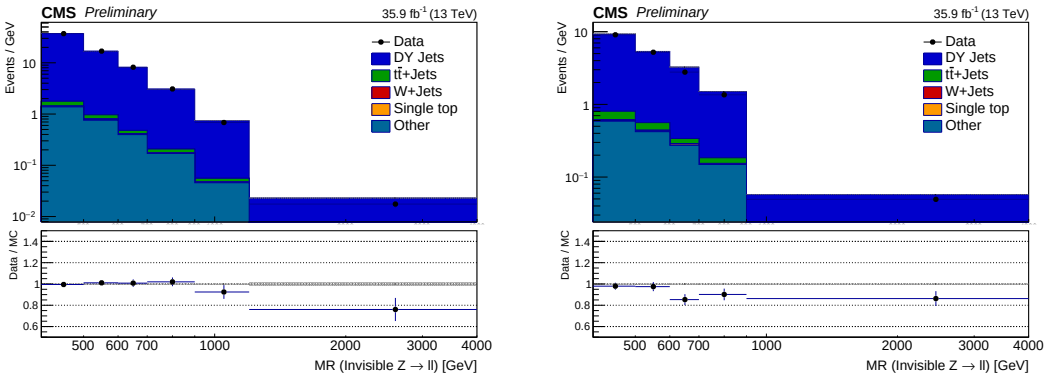

Figure 5: The M_R distribution in the Drell-Yan(DY)+jets dilepton control region is displayed in the 2–3 and 4–6 jet categories along with the corresponding MC predictions. The corrections derived from the γ+jets control region as well as the overall normalization correction have been applied in this figure.

The MC corrections derived in the γ+jets control region are checked against a second set of corrections derived in a control region enriched in $W(\ell\nu)$+jets events. This control region is identical to the $W(\ell\nu)$+jets sample described in Section 5.1, except that the selected lepton is

treated as invisible for the purpose of computing M_R and R^2. Correction factors are derived in the same way as in the $W(\ell\nu)$+jets control region. The full difference between these corrections and those obtained from the γ+jets control region is taken as a systematic uncertainty in the $Z(\nu\bar{\nu})$+jets prediction in the signal region, and is typically between 10% and 20% depending on the bin.

5.3 QCD Multijet Background

QCD multijet events compose a nonnegligible fraction of the total yield in the hadronic search regions. Such events are characterized by a significant under-measurement of the energy of a jet, and consequently a large amount of p_T^{miss}, usually pointing towards the mismeasured jet. A large fraction of QCD multijet events are rejected by the requirement that the azimuthal angle $\Delta\phi_R$ between the axes of the two razor megajets is less than 2.8. We treat the events with $\Delta\phi_R > 2.8$ as a control sample of QCD multijet events.

We estimate the number of QCD multijet events in this control region in bins of M_R and R^2 by subtracting the predicted contribution of other processes from the total event yield in each bin. This is done for each jet multiplicity category. We observe in MC that the fraction of QCD multijet events at each b-tag multiplicity is independent of M_R, R^2, and $\Delta\phi_R$. The event yields in the high $\Delta\phi_R$ region are therefore measured independently of the number of b-tags and scaled according to the fraction of QCD multijet events at each multiplicity of b-tagged jets.

We then predict the number of QCD multijet events in the search region via the transfer factor ζ, defined by

$$\zeta = \frac{N(|\Delta\phi_R| > 2.8)}{N(|\Delta\phi_R| < 2.8)}. \tag{6}$$

In MC we observe that ζ changes slowly with M_R and increases roughly linearly with R^2. In data we therefore compute ζ in bins of M_R and R^2 in a low-R^2 region defined by $0.20 < R^2 < 0.30$ and fit the computed values with a linear function in M_R and R^2. We then use the linear fit and its uncertainty to estimate the value of ζ in the analysis search regions. The fit is performed separately in each category of jet multiplicity, but inclusively in the number of b-tagged jets, as ζ is observed in MC not to depend on the b-tag multiplicity. For the category with seven or more jets the fit function is allowed to depend on R^2 only, due to the low number of events in the fit region.

The statistical uncertainty of the control region event counts and the fitted uncertainty of the transfer factor extrapolation are propagated as systematic uncertainties of the QCD multijet background prediction. Another systematic uncertainty of 30% is propagated in order to cover the dependence of the transfer factor on the number of b-tagged jets in the different control regions. Furthermore, we make an alternative extrapolation for the transfer factor where we allow a dependence on M_R and R^2 for the Seven-jet category, and a quadratic dependence on M_R for the Dijet and Multijet categories. The difference in the QCD multijet background prediction between the default and alternative transfer factor extrapolation is propagated as an additional systematic uncertainty, whose size ranges from 10% for M_R below 1 TeV to 70–90% for M_R above 1.6 TeV.

5.4 Background Modeling in Boosted Event Categories

The dominant SM background processes in the boosted categories are the same as in the non-boosted categories. An additional but important source of background comes from processes

where one of the jets in the event is mistagged as a boosted hadronic W boson or top quark.

Requiring boosted objects in the selection results in a smaller number of events in the signal or control regions. As a generic rule, in cases where no MC events exist in signal region bins for a given background process, MC counts in these bins are extrapolated from a looser version of the signal selection obtained by relaxing the N-subjettiness criteria for W or top jet tagging. For cases where there are no counts or very low statistical precision in the control region bins, these depleted bins are temporarily merged to obtain coarser bins with improved statistics. Background estimation is done in two steps, where first the yields are estimated using the coarser bins, and next, the yields in coarse bins are distributed to the finer bins proportional to the background MC counts in the finer bins.

5.4.1 $\mathrm{t\bar{t}}$+jets and W+jets background estimation for the boosted categories

The control regions for the top quark and W+jets backgrounds are defined similar to the control regions used for the nonboosted categories. We require exactly one veto electron or muon. To suppress contamination from signal processes, M_{T} is required to be less than 100 GeV. To mimic the signal selection, the $\Delta\phi_{\mathrm{R}} < 2.8$ cut is applied. To estimate the top quark background for the Wnj45 and Wnj6 search region categories, we require events in the control region to have at least one boosted W boson and one tagged b jet, while for the Top category, we require one boosted top quark. To estimate the W($\ell\nu$)+jets background for the Wnj45 and Wnj6 search region categories, we require events in the control region to have no loosely tagged bjets, while for the Top category we require no subjet b-tags. To maintain consistency with signal region kinematics, we require a jet which is tagged only using the W or top mass requirement, but without the N-subjettiness requirement. The background estimate for each search region i is then extrapolated from the corresponding control region via transfer factors calculated in MC: $\lambda_{\mathrm{i}} = N_{\mathrm{i}}^{\mathrm{SR,MC}} / N_{\mathrm{i}}^{\mathrm{CR,MC}}$.

For certain bins, the MC prediction of the transfer factors can have large statistical fluctuations due to the limited size of the MC sample. To smooth out these fluctuations we use a combination of bin-merging and extrapolations from a region with looser requirements on the N-subjettiness variables. While the fluctuations of the nominal background prediction are smoothed out, the statistical uncertainties due to limited MC events are still propagated as a systematic uncertainty.

Figure 6 shows the b-tagged jet multiplicity distribution for the Wnj6 category before applying the b-tagging selection, and the M_{T} distribution in the Top category before applying the M_{T} selection. Figure 7 shows the distribution in M_{R} and R^2 bins for events in the Top category in the top quark control region, and for events in the Wnj45, Wnj6 categories in the W($\ell\nu$)+jets control region. The purity of $\mathrm{t\bar{t}}$+jets and single top events in the top quark control region is more than 80%, and the purity of the W($\ell\nu$)+jets process in the W($\ell\nu$)+jets control region is also larger than 80%.

5.4.2 $\mathrm{Z} \to \nu\bar{\nu}$+jets background estimation for the boosted categories

The background estimate for the $\mathrm{Z} \to \nu\bar{\nu}$+jets process is again similar to the method used for the nonboosted categories. We make use the similarity in the kinematics of the photon in γ+jets events and the Z boson in Z+jets events to select a control sample of γ+jets to mimic the behavior of $\mathrm{Z} \to \nu\bar{\nu}$+jets events. The γ+jets control region is selected by requiring exactly one photon with $p_{\mathrm{T}} > 80$ GeV from data collected by jet and H_{T} triggers., The momentum of the photon is added to $\vec{p}_{\mathrm{T}}^{\,\mathrm{miss}}$ to mimic the contribution of the neutrinos from $\mathrm{Z} \to \nu\bar{\nu}$ decays. The lepton veto is applied, and $\Delta\phi_{\mathrm{R}}$, computed after treating the photon as invisible, is required

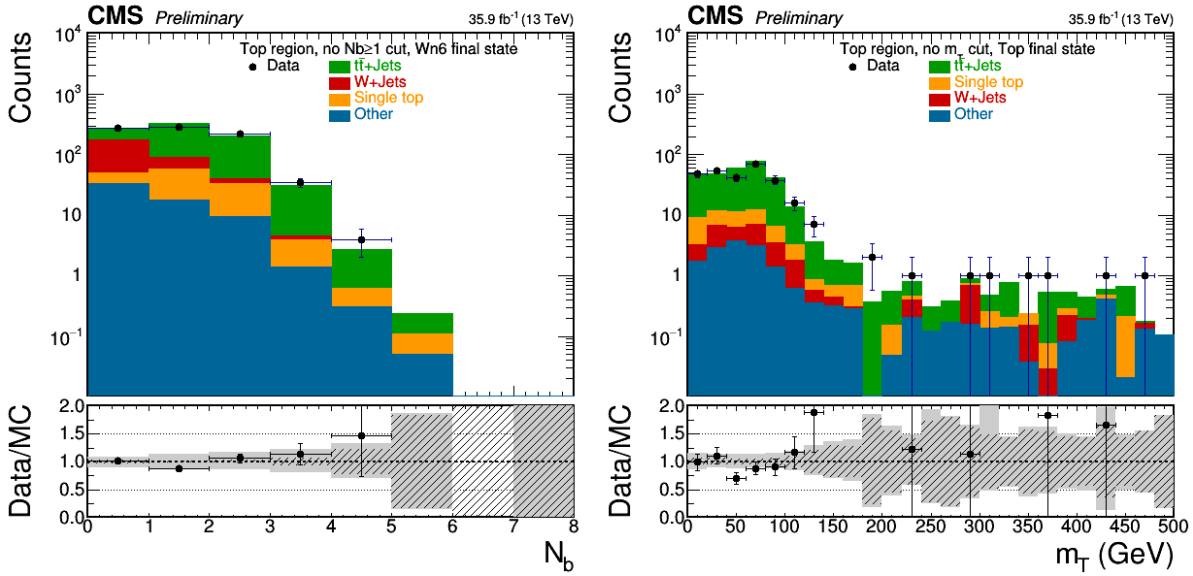

Figure 6: Distributions of b-tagged jet multiplicity before applying the b-tagging selection requirement in the W+jets control region of the boosted Wnj6 category (left), and distributions in M_{T} before applying the M_{T} selection requirement in the top quark control region of the boosted Top category (right) are shown. The ratio of data over MC prediction is shown in the lower panels, where the gray band is the total uncertainty and the dashed band is the statistical uncertainty in the MC prediction.

to be less than 2.8. One mass tagged W jet or top quark jet is required for the W and Top categories respectively. Figure 8 shows the photon p_{T} and M_{R}-R^2 distributions for the Top category. The QCD multijet contribution to the γ+jets control region is accounted for by a template fit to the photon charged isolation variable in inclusive bins of M_{R} and R^2. Other background processes in the γ+jets control regions are small and predicted using MC. Finally, the signal region prediction for the $\mathrm{Z} \to \nu\bar{\nu}$+jets background is extrapolated from the γ+jets yields via the MC transfer factor $\lambda_{\mathrm{Z}\to\nu\bar{\nu}} = N^{\mathrm{SR,MC}}_{\mathrm{Z}\to\nu\bar{\nu}} / N^{\mathrm{CR,MC}}_{\gamma+\mathrm{jets}}$.

We perform a cross check on the previous estimate using a control region enhanced in $\mathrm{Z} \to \ell\ell$ events. The $\mathrm{Z} \to \ell\ell$ control region is defined by requiring exactly two tight electrons or muons with $p_{\mathrm{T}} > 10$ GeV and dilepton mass satisfying $|m_{ll} - m_{\mathrm{Z}}| < 10$ GeV, where m_{Z} is the Z boson mass. All other requirements are the same as those for the γ+jets control region. The momentum of the dilepton system is added vectorially to $\vec{p}_{\mathrm{T}}^{\,\mathrm{miss}}$ to mimic an invisible decay of the Z boson. Similar to the procedure for the nonboosted categories, the comparison between data and MC yields in the $\mathrm{Z} \to \ell\ell$ control region are used to correct the MC transfer factor λ to account for the impact of missing higher order corrections on the total normalization predicted by the γ+jets MC.

As for the inclusive categories, we obtain an alternative estimate from the $W(\to l\nu)$+jets enriched control region to validate the predictions from the γ+jets control region. We require the presence of exactly one tight electron or muon. M_{T} is required to be between 30 to 100 GeV. The rest of the selection is the same as for the γ+jets control region. The lepton momentum is added vectorially to $\vec{p}_{\mathrm{T}}^{\,\mathrm{miss}}$ to mimic an invisible decay. The $W(\to l\nu)$+jets control region yields are extrapolated to the signal region via transfer factors calculated from MC to obtain the alternative $\mathrm{Z} \to \nu\bar{\nu}$+jets background estimate. Figure 9 compares the estimates from the γ+jets control region, the $W(\to l\nu)$+jets control region, and the MC simulation. The difference between the two alternative data-driven estimates is propagated as a systematic uncertainty.

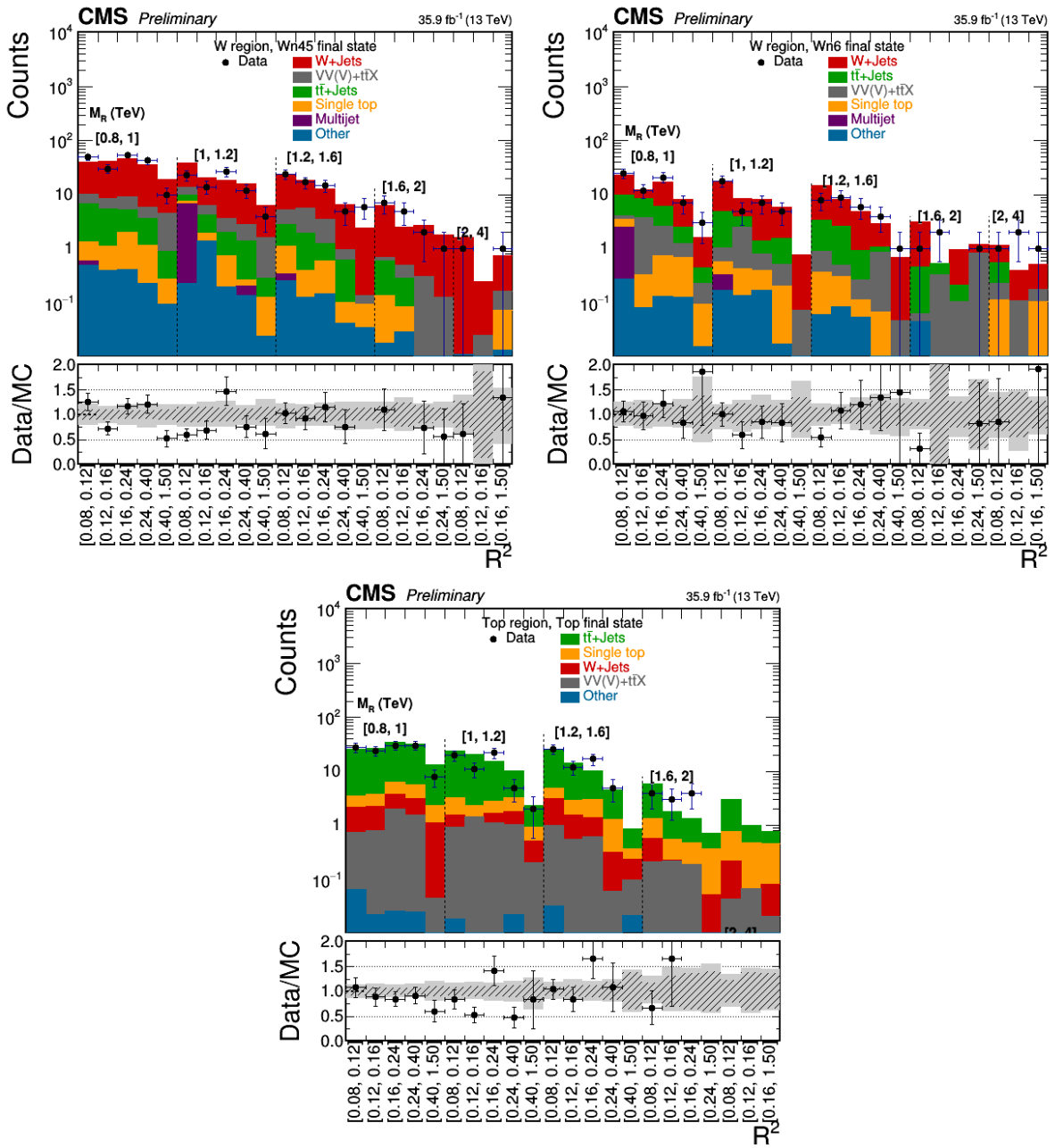

Figure 7: M_R-R^2 distributions in the W+jets control regions of the boosted Wnj45 and Wnj6 categories, and the top quark control region of the Top category. The ratio of data over MC prediction is shown in the lower panels, where the gray band is the total uncertainty and the dashed band is the statistical uncertainty in the MC prediction.

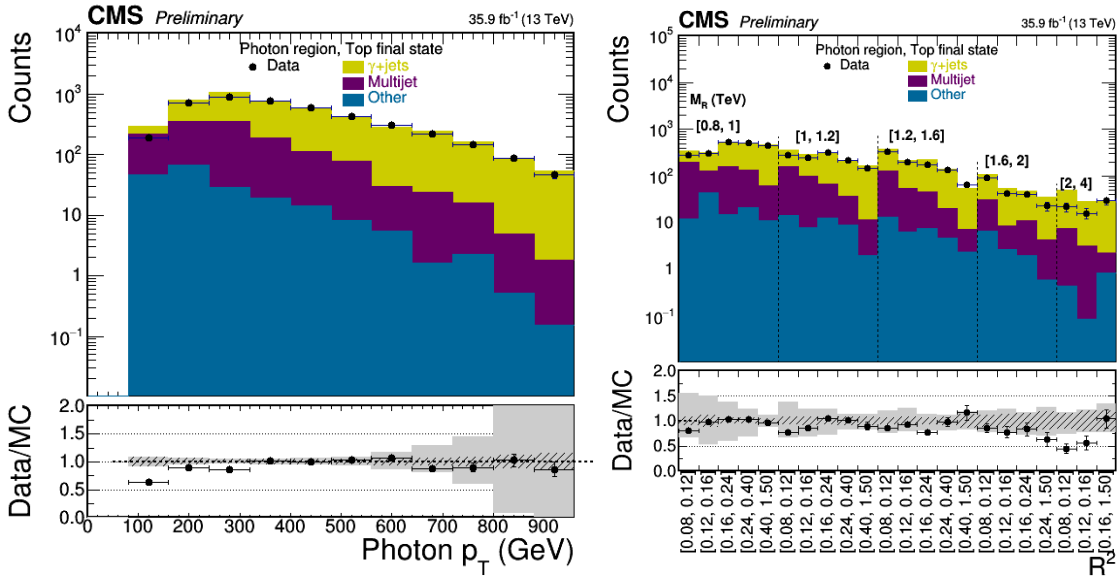

Figure 8: Photon p_T and M_R-R^2 distributions for the γ+jets control regions of the boosted Top category. The ratio of data over MC prediction is shown in the lower panels, where the gray band is the total uncertainty and the dashed band is the statistical uncertainty in the MC prediction.

5.4.3 Multijet background estimation in the boosted categories

The control region enriched in QCD multijet background is defined by inverting the $\Delta\phi_R$ requirement, and requiring anti-tagged W boson or top quark candidates by inverting the N-subjettiness criteria and subjet b-tagging for top jets. Figure 10 shows the distribution in the M_R and R^2 bins for the Wnj45, Wnj6 and Top categories. The purity achieved with the selection described above is about 90%. The QCD multijet background is predicted by extrapolating the event yields from this QCD multijet control region to the search regions via transfer factors calculated from MC.

The effects of inaccuracies in the QCD multijet MC modeling on the multijet background estimate are taken into account by propagating a systematic uncertainty computed based on the level of disagreement between data and MC in the b jet multiplicity, N-subjettines and $\Delta\phi_R$ distributions before applying these selections. The resulting overall systematic uncertainties are 13% and 24% for W and Top categories respectively.

5.4.4 Validating background estimation with closure tests in boosted categories

Two validations are performed in control regions similarly to the QCD multijet control region but inverting only one of the two requirements. These validations are intended to verify the reliability of the data-driven background estimates for the boosted categories.

The first validation is performed in a control region that is defined identically to the search region except that we invert the $\Delta\phi_R$ requirement. The comparison between data and predicted background validates the MC modeling of b-tagging, the $\Delta\phi_R$ shape, the extrapolation in the lepton multiplicity, and the accuracy of the efficiency for W boson and top quark tagging. Figure 11 shows the results for the Wnj35, Wnj6, W combined, and Top categories. Overall, the estimation agrees with data within uncertainties.

The second validation is performed in a control region defined identically to the search region but requiring anti-tagged W boson or top quark candidates. This validation is designed to

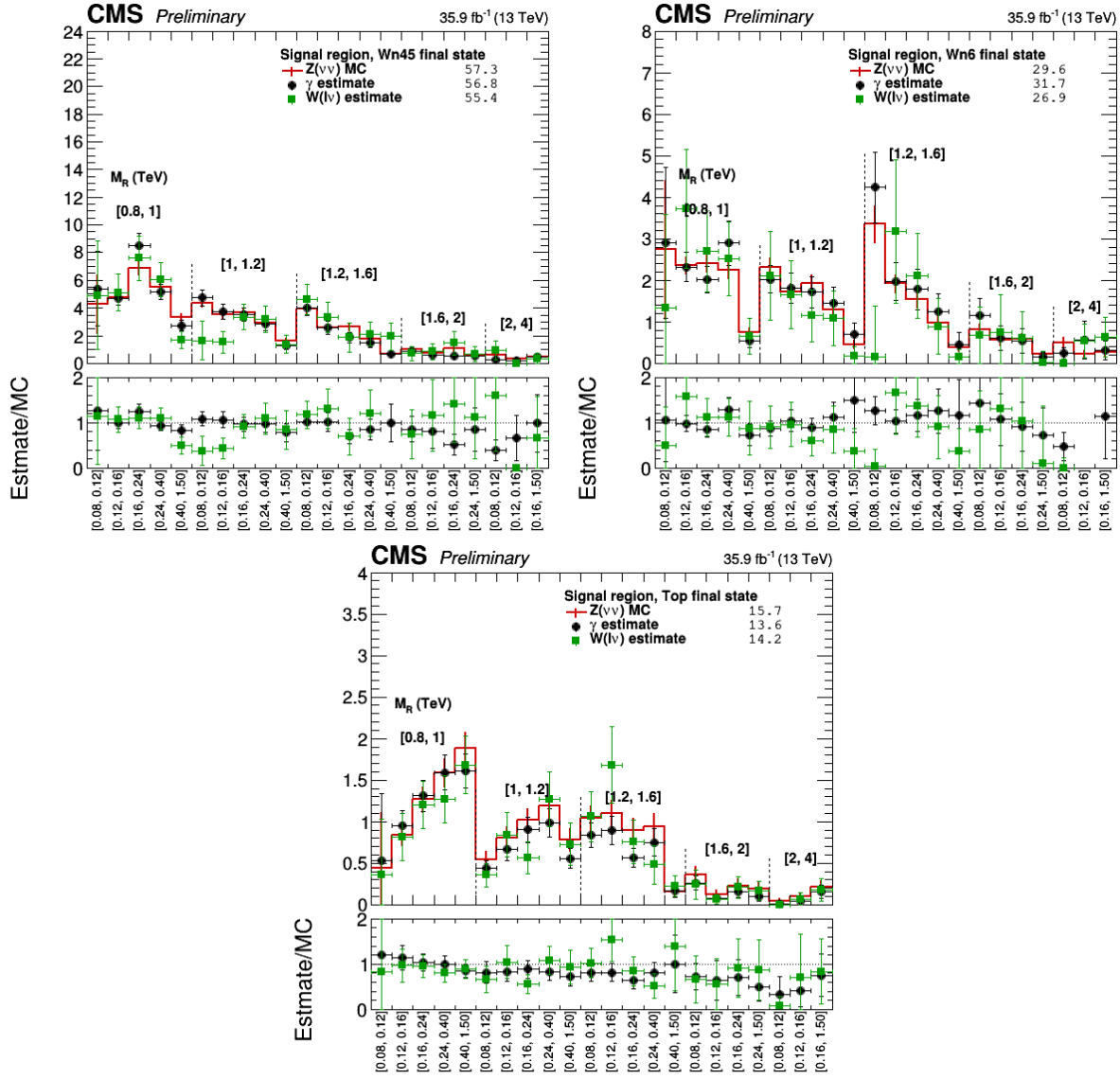

Figure 9: Comparison of the estimation of the $Z(\rightarrow \nu\nu)$+jets background contribution in the search region extrapolated from the γ+jets control region with the estimation extrapolated from the $W(\rightarrow l\nu)$+jets control region for the boosted Wnj45, Wnj6 and Top categories. The prediction from the uncorrected MC simulation is also shown.

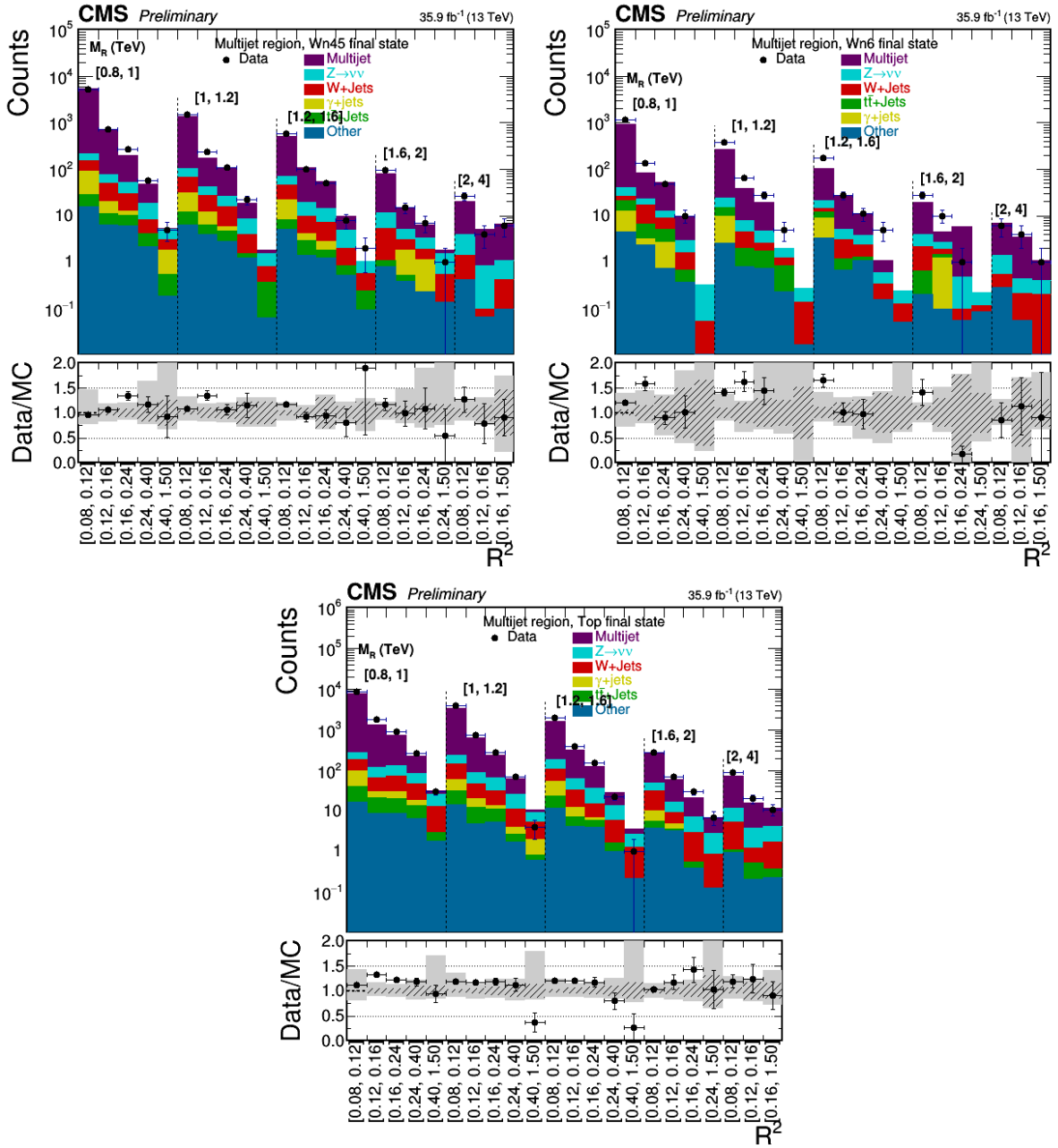

Figure 10: M_R-R^2 distributions in the QCD multijet control regions of the Wnj45 (upper left), Wnj6 (upper right) and Top (bottom) categories. The ratio of data over MC prediction is shown in the lower panels, where the gray band is the total uncertainty and the dashed band is the statistical uncertainty on the MC prediction.

check the modeling of the $\Delta\phi_R$ variable in the QCD multijet and $Z(\nu\bar{\nu})$+jets MC. The plots in Figure 12 show the estimation results compared to data for the Wnj45, Wnj6 and Top categories. Overall, the estimation agrees with data within uncertainties.

6 Systematic Uncertainties

Systematic uncertainties propagated in this analysis can be broadly categorized into three types. The first type are systematic uncertainties due to the limited accuracy of calibrations, efficiency measurements, and theoretical predictions. These are propagated as shape uncertainties in the signal and background predictions in all event categories. Uncertainties in the trigger and lepton selection efficiency, and on the integrated luminosity, primarily affect the total normalization. Uncertainties in the b-tagging efficiency affect the relative yields between different b-tag categories. Systematic uncertainties in the modeling of the W boson and top quark tagging and mistagging efficiencies affect the yields of the boosted categories. The uncertainties from missing higher order corrections and the uncertainties in the jet energy and lepton momentum scale affect the shapes of the M_R and R^2 distributions. In Table 3 we summarize these systematic uncertainties and their typical impact on background and signal predictions.

Table 3: Summary of the main instrumental and theoretical systematic uncertainties.

Systematic Uncertainty Source	On Signal and/or Bkg	Typical Impact of Uncertainty on Yields (%)
Jet Energy Scale	Both	6–16
Lepton Momentum Scale	Both	1
Muon efficiency	Both	1
Electron efficiency	Both	1–2
Trigger efficiency	Both	1
b-tagging efficiency	Both	1–7
b mistagging efficiency	Both	2–20
W/top-tagging efficiency	Both	1–8
W/top mistagging efficiency	Both	1–3
Higher-Order Corrections	Both	10–25
Luminosity	Both	2.6
Pileup	Both	1–3
Monte Carlo Statistics	Both	1–50
Fast Simulation corrections	Signal only	1–5
Initial State Radiation	Signal only	4–25

The second type of systematic uncertainty is related to the data-driven background prediction methodology. Statistical uncertainties of the control region data range from $1-20\%$ depending on the M_R and R^2 bin. Systematic uncertainties of the background processes that we are not targeting in each control region contribute at the level of a few percent. Systematic uncertainties related to the accuracy of assumptions made by the background estimation method are estimated through closure tests in different control regions as discussed in Section 5. These systematic uncertainties capture the potential modeling inadequacies of the MC after applying the corrections derived as part of the analysis procedure. They are summarized in Table 4.

For the closure tests performed in each N_{jets} bin in the $t\bar{t}$ dilepton and the $Z(\nu\bar{\nu})$+jets dilepton control regions, and the test of the p_T distributions in the veto lepton and tau control regions, the uncertainties are applied correlated across all bins. For the checks of the R^2 distributions in

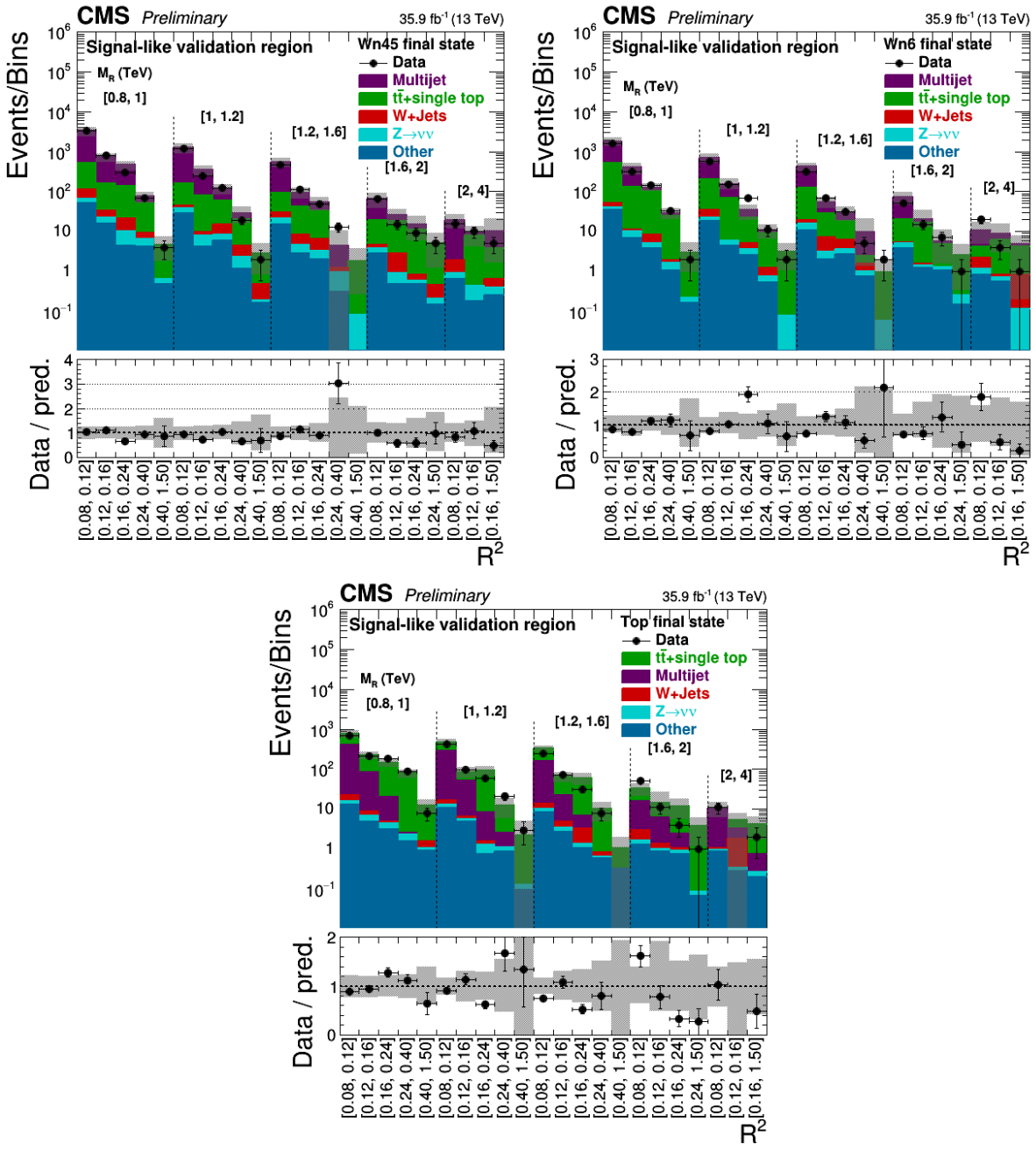

Figure 11: Comparisons between data and the predicted background for the inverted $\Delta\phi_R$ validation region for the boosted Wnj45 (upper left), Wnj6 (upper right) and Top (bottom) categories.

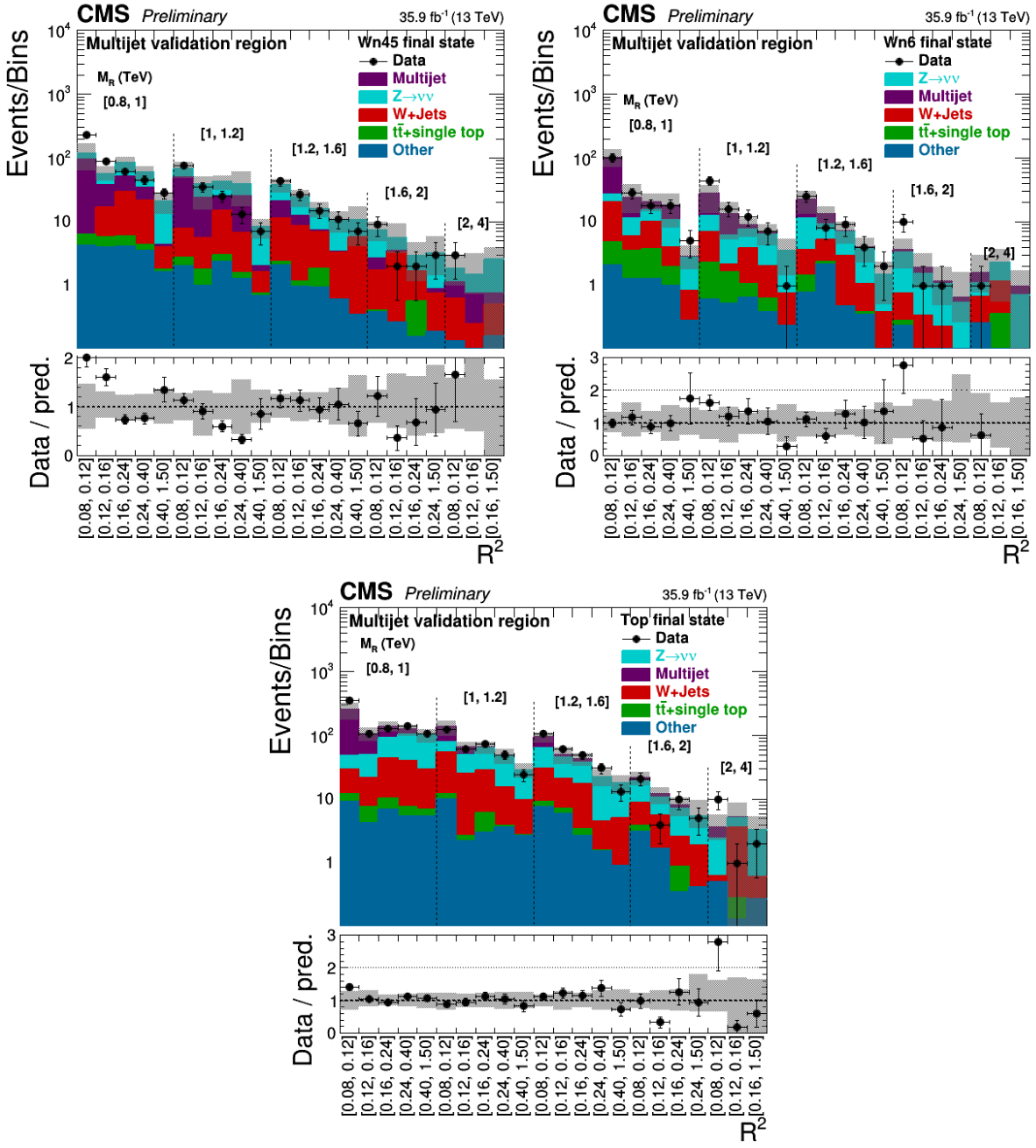

Figure 12: Comparisons between data and the predicted background for the validation region with anti-tagged W boson or top quark candidates for the boosted Wnj45 (upper left), Wnj6 (upper right) and Top (bottom) categories.

each b-tag category in the one-lepton and photon control regions, and of the lepton η distributions in the veto lepton and tau control regions, the systematic uncertainties are assigned based on the size of the statistical uncertainty in the control regions and are uncorrelated from bin to bin.

For the $Z(\nu\bar{\nu})$+jets process, the difference in the correction factors computed in the γ+jets and one-lepton control regions are propagated as a systematic uncertainty. This systematic uncertainty estimates the potential differences in the MC mismodeling of the hadronic recoil between the γ+jets process and the $Z(\nu\bar{\nu})$+jets process. These systematic uncertainties range up to 20%.

Table 4: Summary of systematic uncertainties due to background estimation methodology expressed as relative or fractional uncertainties.

Uncertainty Source	Background Process	Size (%)
Non-Boosted categories		
1-lepton CR, R^2 closure test	$t\bar{t}$, W+jets	1–95
$t\bar{t}$ 2-lepton closure test	$t\bar{t}$	1–12
Veto lepton p_T closure test	$t\bar{t}$, W+jets	4–50
Veto lepton η closure test	$t\bar{t}$, W+jets	5–40
Veto tau p_T closure test	$t\bar{t}$, W+jets	2–43
Veto tau η closure test	$t\bar{t}$, W+jets	2–28
γ+jets CR, R^2 closure test	$Z(\nu\bar{\nu})$+jets	1–40
DY+jets 2-lepton closure test	$Z(\nu\bar{\nu})$+jets	1–25
QCD Multijet transfer factor extrapolation	QCD Multijet	30–90
Boosted categories		
QCD Multijet modeling	QCD Multijet	13–24
DY+jets modeling	$Z(\nu\bar{\nu})$+jets	19–29
$Z(\nu\bar{\nu})$+jets closure test	$Z(\nu\bar{\nu})$+jets	19–98

Finally, there are systematic uncertainties specific to the fast simulation prediction of the signal. These include systematic uncertainties due to possible inaccuracies of the fast simulation in modeling the efficiencies for lepton selection, b-tagging, and boosted W boson and top quark tagging. To correct for possible mismodeling of the signal acceptance due to differences in the data and signal MC pileup distributions, we employ a linear fit that extrapolates the acceptance in each analysis bin to the range of pileup values observed in data. Uncertainty in this method is propagated to the signal yield predictions. An additional uncertainty is applied to correct for known tendencies for the fast simulation to mismodel the p_T^{miss} in some events. Finally, we propagate an uncertainty in the modeling of initial state radiation for signal predictions, ranging from 4–25% depending on the number of jets from initial state radiation.

7 Results and interpretation

The observed data yields in the search regions are statistically compatible with the background prediction from SM processes. The results are summarized in the distributions of the M_R and R^2 bins of the search regions. The results for the one-lepton categories are shown in Figures 13-16. The main backgrounds are W+jets and $t\bar{t}$ with $t\bar{t}$ becoming more dominant with increasing number of b-tagged jets. The three example signals used to interpret the results are also shown.

The results for the zero-lepton boosted categories are shown in Figure 17, where $t\bar{t}$ is the dominant background process in all subcategories.

Finally, the results for the zero-lepton nonboosted categories are shown in Figures 18-23. The $Z(\nu\bar{\nu})$+jets background is dominant for subcategories with fewer jets and b-tagged jets, while the $t\bar{t}$ background is dominant for subcategories with more jets and b-tagged jets.

In the absence of observed statistically significant excesses in the data, we proceed to interpret the results of the search in terms of upper limits on the production cross sections of various SUSY simplified models. We follow the LHC CL_s procedure [73] by using the profile likelihood ratio test statistic and the asymptotic formula to evaluate the 95% CL observed and expected limits on the production cross section. Systematic uncertainties are propagated by incorporating nuisance parameters that represent different sources of systematic uncertainty, which are profiled in the maximum likelihood fit.

We focus on simplified models for which this analysis has enhanced sensitivity compared to alternative searches. The corresponding Feynman diagrams for the simplified models that we consider are shown in Figure 24. Generically, the best signal sensitivity comes from the Lepton MultiJet and Multijet categories, and are dominated by bins with large M_R when the mass splitting between the gluino (or squark) and the LSP is large, and by bins with large R^2 when the mass splitting is small. For signal models that produce many jets, like gluino pair production decaying to two top quarks and the LSP, the Lepton Seven-jet and Seven-jet categories dominate the sensitivity. For signal models with boosted top quarks, such as top squark pair production, the boosted categories contribute significantly to the sensitivity.

First, we consider the scenario of pair produced gluinos decaying to quarks. The expected and observed limits for gluinos decaying to a pair of top quarks and the LSP are shown as a function of gluino and LSP masses in Figure 25. In this simplified model, we exclude gluino masses up to 2.0 TeV for LSP mass below 700 GeV. The limit for gluinos decaying to a top quark and a low mass top squark, which subsequently decays to a charm quark and the LSP, is shown in Figure 26. For this simplified model, we exclude gluino masses up to 1.9 TeV for LSP mass above 150 GeV and below 950 GeV, extending the previous best limits [74] from the CMS experiment by about 100 GeV in the gluino mass. Finally, we consider pair produced top squarks decaying to the top quark and the LSP. The expected and observed limits are shown in Figure 27, and we exclude top squark masses up to 1.14 TeV for LSP mass below 200 GeV, extending the previous best limits [27] from the CMS experiment by about 20 GeV. The dotted blue contour in each exclusion limit plot represents the expected limit obtained using data from the nonboosted categories only. By comparing the difference between the expected limits obtained using only the nonboosted categories with the expected limits using all categories, we observe clearly that the boosted categories make an important contribution to the sensitivity for the signal models presented here.

8 Summary

We have presented an inclusive search for supersymmetry in events with no more than one lepton, a large multiplicity of energetic jets, and evidence of invisible particles using the razor kinematic variables. To enhance sensitivity to a broad range of signal models, the events are categorized according to the number of leptons, the presence of jets consistent with hadronically decaying W bosons or top quarks, and the number of jets and b-tagged jets. This analysis is the first inclusive search for supersymmetry from the CMS experiment that explicitly incorporates event categories with boosted W boson or top quark jets. The analysis uses 35.9 fb^{-1} of $\sqrt{s} = 13$ TeV proton-proton collision data collected by the CMS experiment. Standard model backgrounds were estimated using control regions in data and Monte Carlo simulation yields

in signal and control regions. Background estimation procedures were verified using validation regions with kinematics resembling that of the signal regions and closure tests. Data are observed to be consistent with the SM expectation.

The search is sensitive to a broad range of SUSY scenarios including pair production of gluinos and top squarks, and the event categorization in the number of leptons, the number of jets and b-tagged jets, and the presence or absence of boosted jets consistent with hadronic W or top decays, enhances the signal to background and search sensitivity simultaneously for a variety of different SUSY signal scenarios.

The results were interpreted in the context of simplified models of gluino pair production decaying to various quark flavors, or direct top squark pair production. Limits on the gluino mass extend to 2.0 TeV while limits on top squark masses reach 1.14 TeV. The advantage of combining a large variety of final states enabled this analysis to improve the sensitivity in various signal scenarios. The analysis extended the exclusion limit of the gluino mass from the CMS experiment by $\sim$ 100 GeV in decays to a low mass top squark and a top quark, and the exclusion limit of the top squark mass by $\sim$ 20 GeV in direct top squark production.

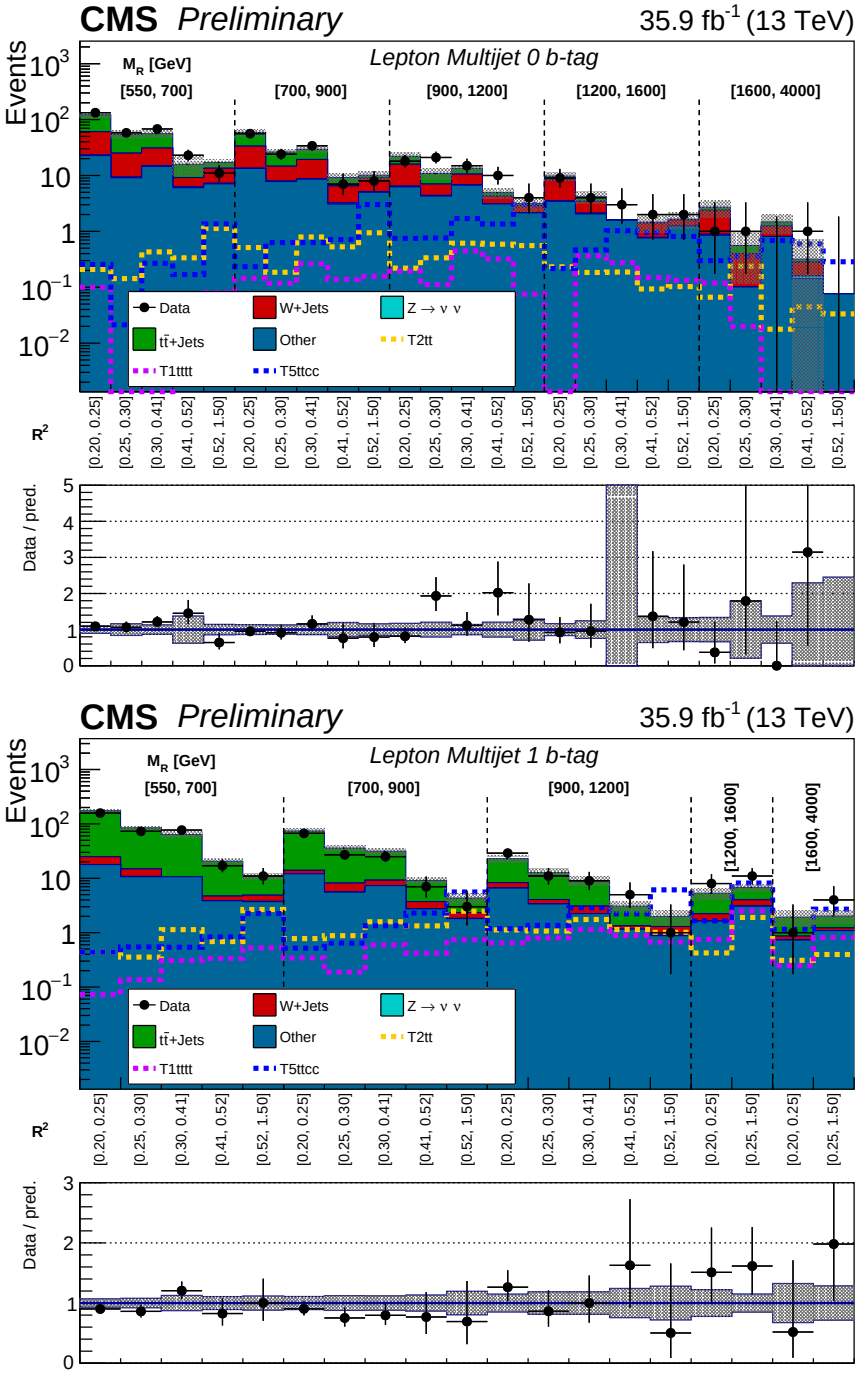

Figure 13: The M_R-R^2 distribution observed in data is shown along with the background prediction obtained for the Lepton Multijet event category in the 0 b-tag (top) and 1 b-tag (bottom) bins. The two-dimensional M_R-R^2 distribution is shown in a one dimensional representation, with each M_R bin marked by the dashed lines and labeled near the top, and each R^2 bin labeled below. The ratio of data to the background prediction is shown on the bottom inset, with the statistical uncertainty expressed through the data point error bars and the systematic uncertainty of the background prediction represented by the shaded region. Signal benchmarks shown are T5ttcc with $m_{\tilde{g}} = 1.4$ TeV, $m_{\tilde{t}} = 320$ GeV and $m_{\tilde{\chi}^0_1} = 300$ GeV; T1tttt with $m_{\tilde{g}} = 1.4$ TeV and $m_{\tilde{\chi}^0_1} = 300$ GeV; and T2tt with $m_{\tilde{t}} = 850$ GeV and $m_{\tilde{\chi}^0_1} = 100$ GeV. The diagrams corresponding to these signal models are shown in Figure 24.

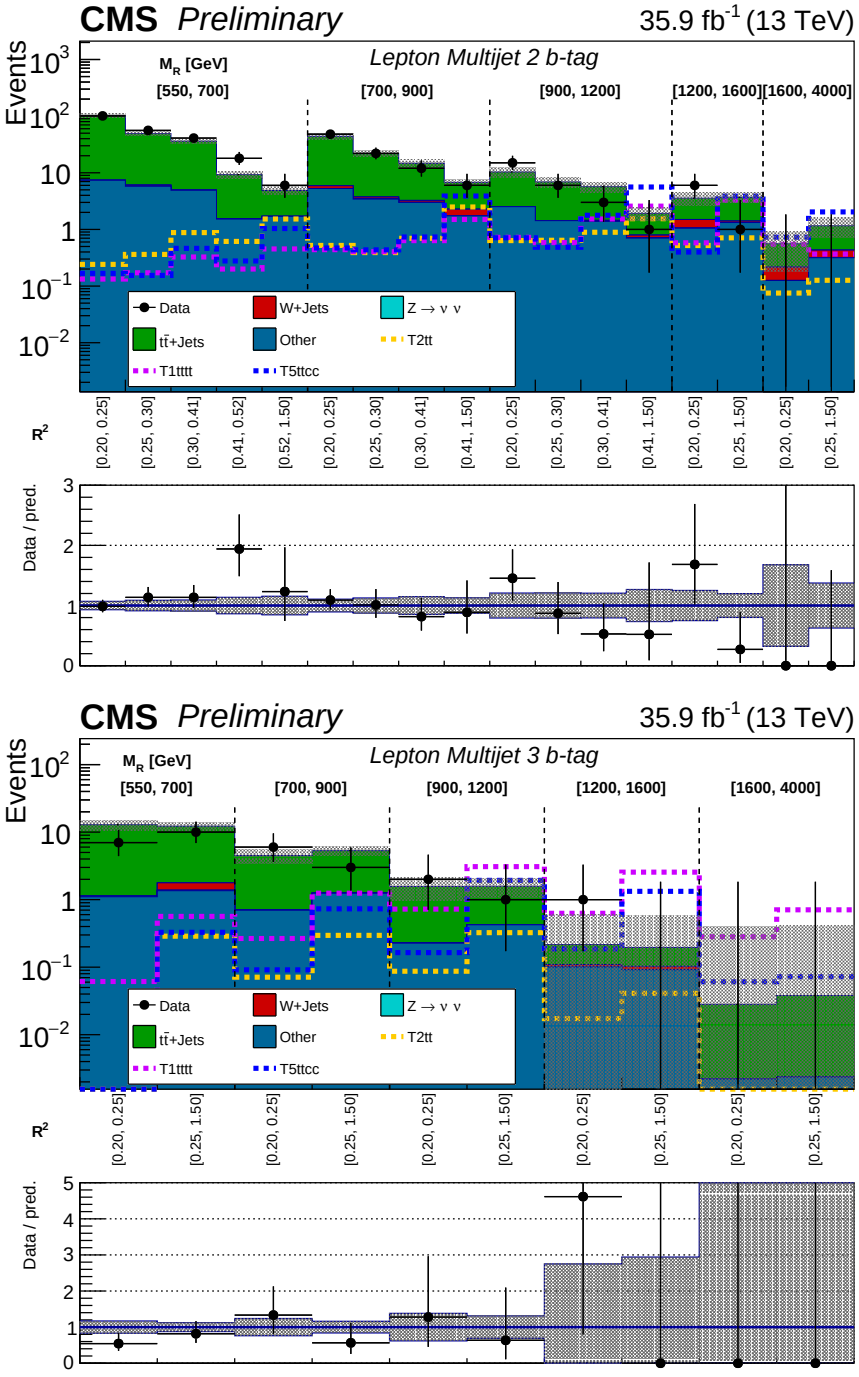

Figure 14: The M_R-R^2 distribution observed in data is shown along with the background prediction obtained for the Lepton Multijet event category in the 2 b-tag (top) and 3 b-tag (bottom) bins. The two-dimensional M_R-R^2 distribution is shown in a one dimensional representation, with each M_R bin marked by the dashed lines and labeled near the top, and each R^2 bin labeled below. The ratio of data to the background prediction is shown on the bottom inset, with the statistical uncertainty expressed through the data point error bars and the systematic uncertainty of the background prediction represented by the shaded region. Signal benchmarks shown are T5ttcc with $m_{\tilde{g}} = 1.4$ TeV, $m_{\tilde{t}} = 320$ GeV and $m_{\tilde{\chi}^0_1} = 300$ GeV; T1tttt with $m_{\tilde{g}} = 1.4$ TeV and $m_{\tilde{\chi}^0_1} = 300$ GeV; and T2tt with $m_{\tilde{t}} = 850$ GeV and $m_{\tilde{\chi}^0_1} = 100$ GeV. The diagrams corresponding to these signal models are shown in Figure 24.

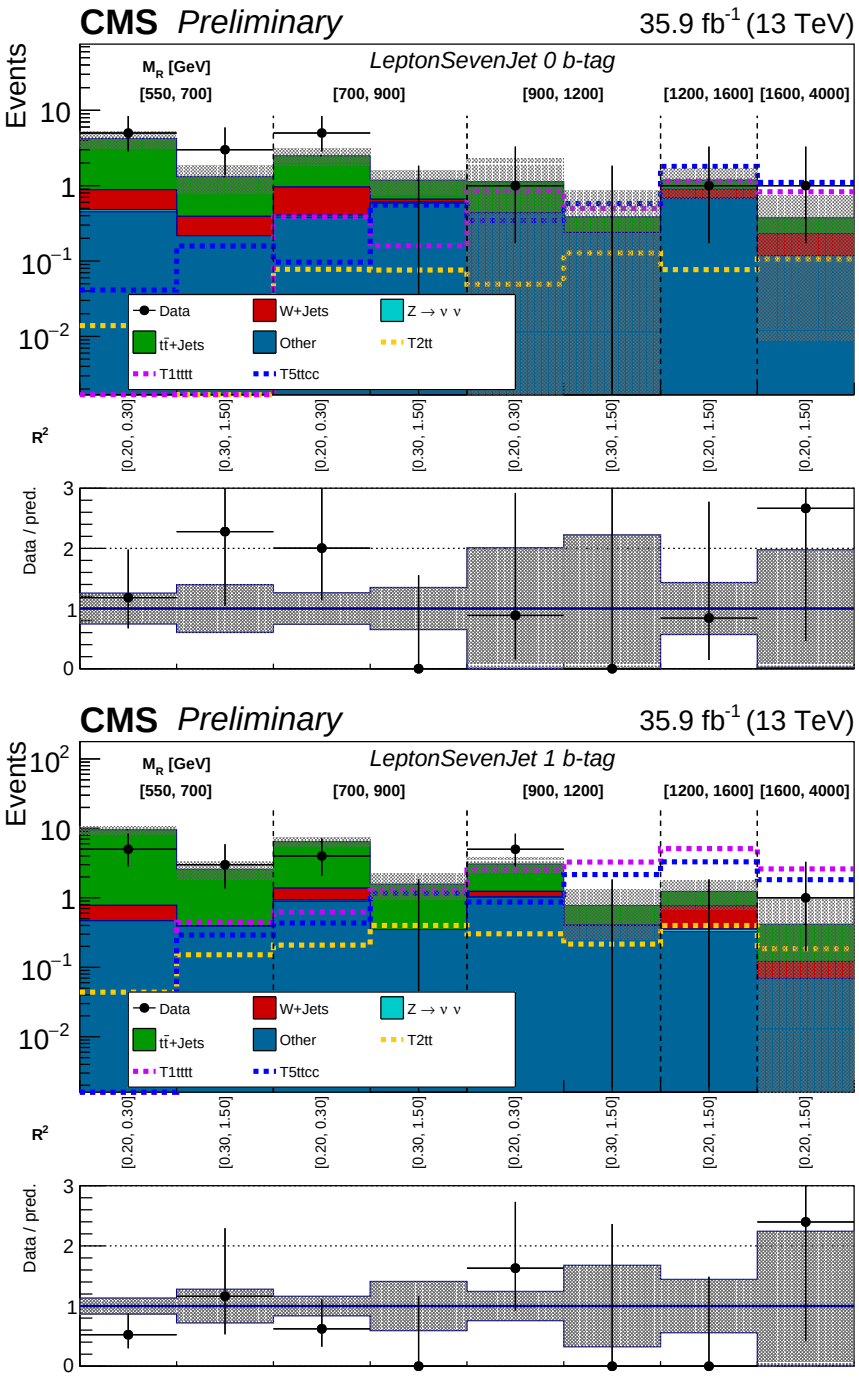

Figure 15: The M_R-R^2 distribution observed in data is shown along with the background prediction obtained for the Lepton Seven-jet event category in the 0 b-tag (top) and 1 b-tag (bottom) bins. The two-dimensional M_R-R^2 distribution is shown in a one dimensional representation, with each M_R bin marked by the dashed lines and labeled near the top, and each R^2 bin labeled below. The ratio of data to the background prediction is shown on the bottom inset, with the statistical uncertainty expressed through the data point error bars and the systematic uncertainty of the background prediction represented by the shaded region. Signal benchmarks shown are T5ttcc with $m_{\tilde{g}} = 1.4$ TeV, $m_{\tilde{t}} = 320$ GeV and $m_{\tilde{\chi}^0_1} = 300$ GeV; T1tttt with $m_{\tilde{g}} = 1.4$ TeV and $m_{\tilde{\chi}^0_1} = 300$ GeV; and T2tt with $m_{\tilde{t}} = 850$ GeV and $m_{\tilde{\chi}^0_1} = 100$ GeV. The diagrams corresponding to these signal models are shown in Figure 24.

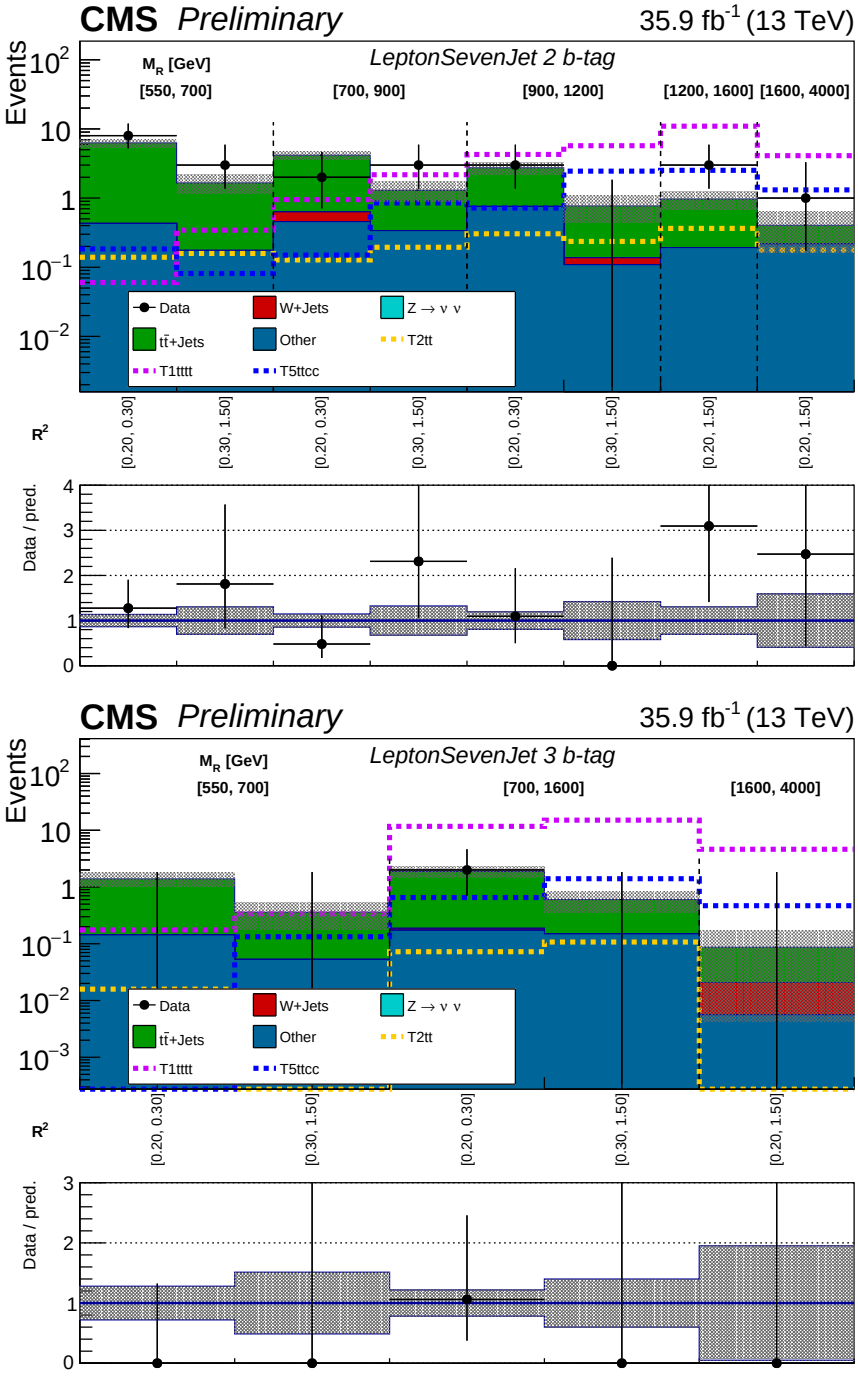

Figure 16: The M_R-R^2 distribution observed in data is shown along with the background prediction obtained for the Lepton Seven-jet event category in the 2 b-tag (top) and 3 b-tag (bottom) bins. The two-dimensional M_R-R^2 distribution is shown in a one dimensional representation, with each M_R bin marked by the dashed lines and labeled near the top, and each R^2 bin labeled below. The ratio of data to the background prediction is shown on the bottom inset, with the statistical uncertainty expressed through the data point error bars and the systematic uncertainty of the background prediction represented by the shaded region. Signal benchmarks shown are T5ttcc with $m_{\tilde{g}} = 1.4$ TeV, $m_{\tilde{t}} = 320$ GeV and $m_{\tilde{\chi}^0_1} = 300$ GeV; T1tttt with $m_{\tilde{g}} = 1.4$ TeV and $m_{\tilde{\chi}^0_1} = 300$ GeV; and T2tt with $m_{\tilde{t}} = 850$ GeV and $m_{\tilde{\chi}^0_1} = 100$ GeV. The diagrams corresponding to these signal models are shown in Figure 24.

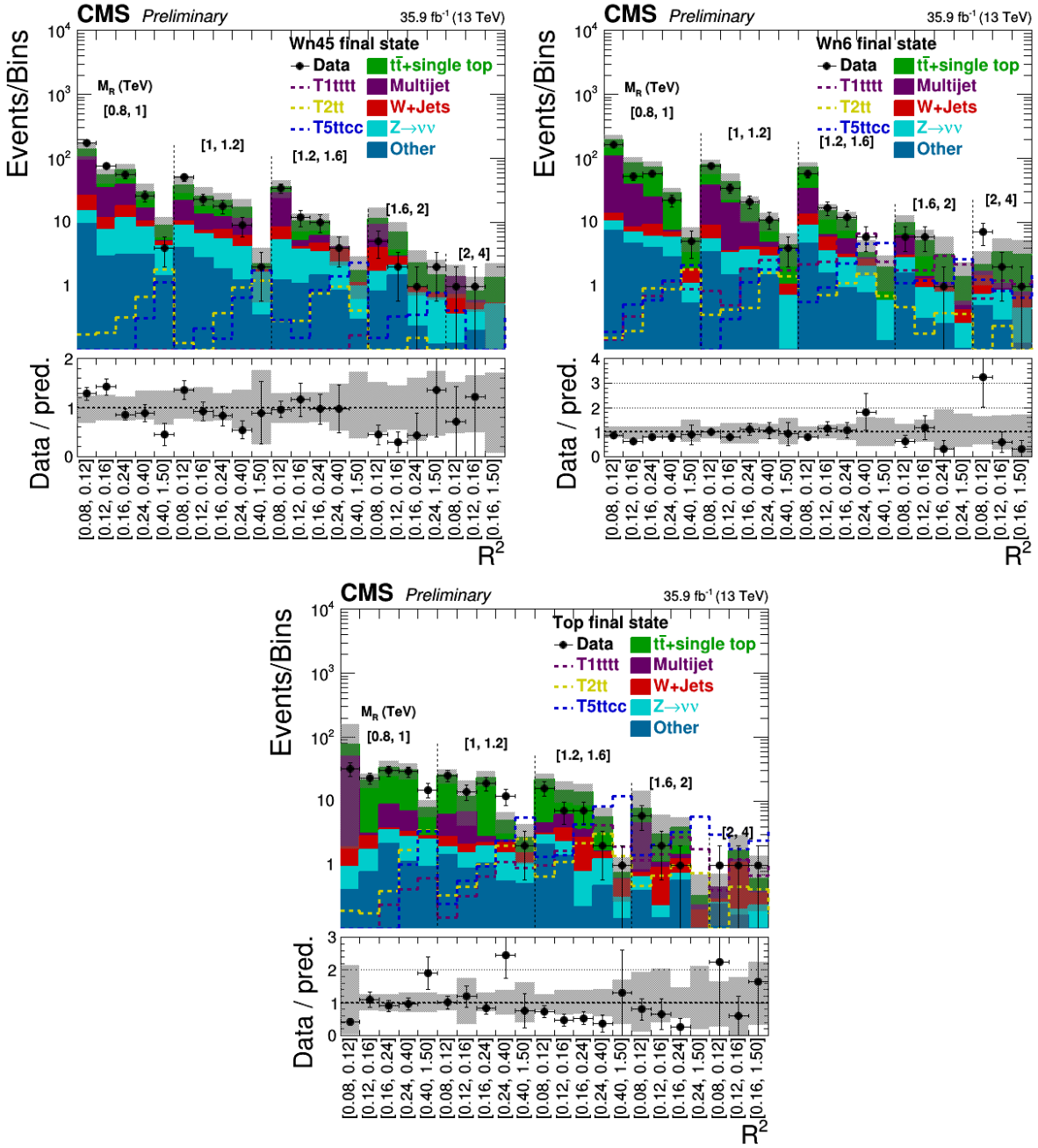

Figure 17: The M_R-R^2 distribution observed in data is shown along with the background prediction obtained for the boosted Wnj45 (upper left), Wnj6 (upper right), and Top (bottom) categories. The two-dimensional M_R-R^2 distribution is shown in a one dimensional representation.The ratio of data to the background prediction is shown on the bottom inset, with the statistical uncertainty expressed through the data point error bars and the systematic uncertainty of the background prediction represented by the shaded region. Signal benchmarks shown are T5ttcc with $m_{\tilde{g}} = 1.4$ TeV, $m_{\tilde{t}} = 320$ GeV and $m_{\tilde{\chi}^0_1} = 300$ GeV; T1tttt with $m_{\tilde{g}} = 1.4$ TeV and $m_{\tilde{\chi}^0_1} = 300$ GeV; and T2tt with $m_{\tilde{t}} = 850$ GeV and $m_{\tilde{\chi}^0_1} = 100$ GeV. The diagrams corresponding to these signal models are shown in Figure 24.

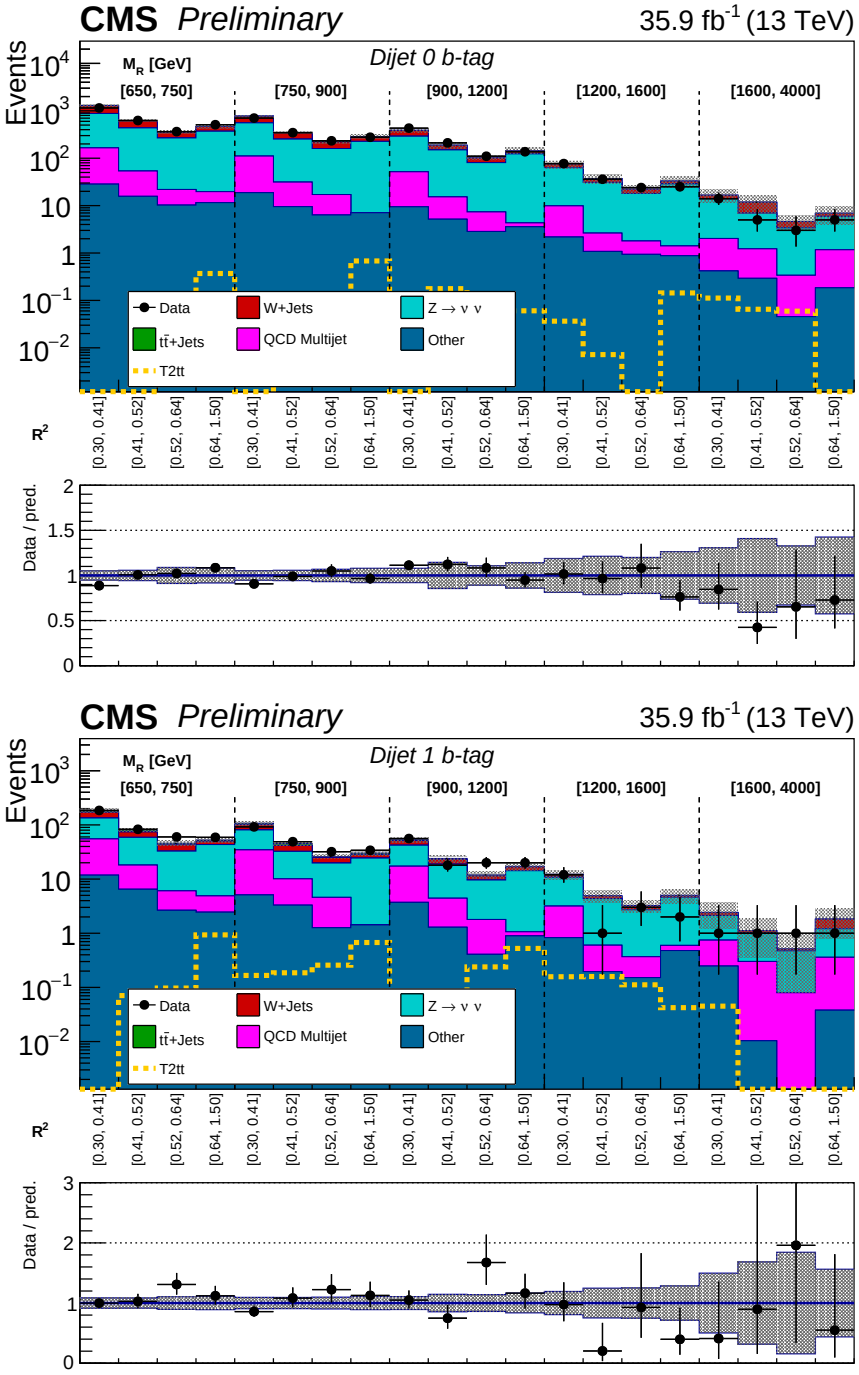

Figure 18: The M_R-R^2 distribution observed in data is shown along with the background prediction obtained for the Dijet event category in the 0 b-tag (top) and 1 b-tag (bottom) bins. The two-dimensional M_R-R^2 distribution is shown in a one dimensional representation, with each M_R bin marked by the dashed lines and labeled near the top, and each R^2 bin labeled below. The ratio of data to the background prediction is shown on the bottom inset, with the statistical uncertainty expressed through the data point error bars and the systematic uncertainty of the background prediction represented by the shaded region. Signal benchmarks shown are T5ttcc with $m_{\tilde{g}} = 1.4$ TeV, $m_{\tilde{t}} = 320$ GeV and $m_{\tilde{\chi}^0_1} = 300$ GeV; T1tttt with $m_{\tilde{g}} = 1.4$ TeV and $m_{\tilde{\chi}^0_1} = 300$ GeV; and T2tt with $m_{\tilde{t}} = 850$ GeV and $m_{\tilde{\chi}^0_1} = 100$ GeV. The diagrams corresponding to these signal models are shown in Figure 24.

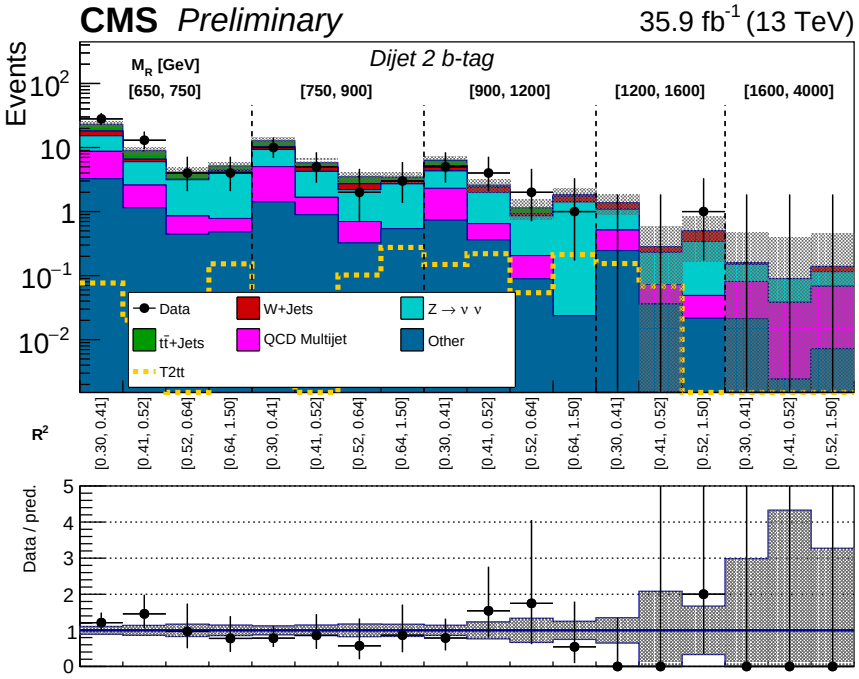

Figure 19: The M_R-R^2 distribution observed in data is shown along with the background prediction obtained for the Dijet event category in the 2 b-tag bin. The two-dimensional M_R-R^2 distribution is shown in a one dimensional representation, with each M_R bin marked by the dashed lines and labeled near the top, and each R^2 bin labeled below. The ratio of data to the background prediction is shown on the bottom inset, with the statistical uncertainty expressed through the data point error bars and the systematic uncertainty of the background prediction represented by the shaded region. Signal benchmarks shown are T5ttcc with $m_{\tilde{g}} = 1.4$ TeV, $m_{\tilde{t}} = 320$ GeV and $m_{\tilde{\chi}_1^0} = 300$ GeV; T1tttt with $m_{\tilde{g}} = 1.4$ TeV and $m_{\tilde{\chi}_1^0} = 300$ GeV; and T2tt with $m_{\tilde{t}} = 850$ GeV and $m_{\tilde{\chi}_1^0} = 100$ GeV. The diagrams corresponding to these signal models are shown in Figure 24.

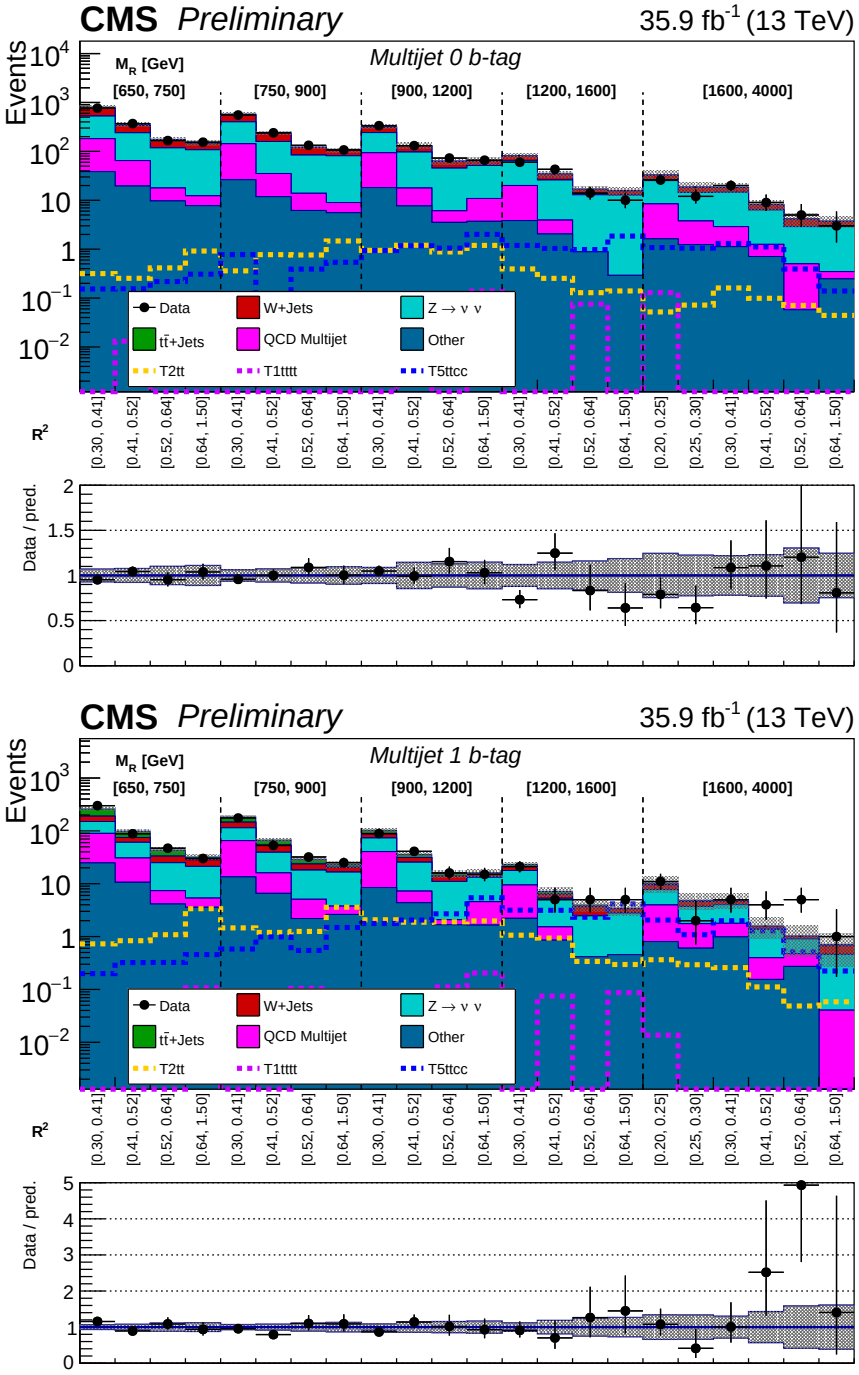

Figure 20: The M_R-R^2 distribution observed in data is shown along with the background prediction obtained for the Multijet event category in the 0 b-tag (top) and 1 b-tag (bottom) bins. The two-dimensional M_R-R^2 distribution is shown in a one dimensional representation, with each M_R bin marked by the dashed lines and labeled near the top, and each R^2 bin labeled below. The ratio of data to the background prediction is shown on the bottom inset, with the statistical uncertainty expressed through the data point error bars and the systematic uncertainty of the background prediction represented by the shaded region. Signal benchmarks shown are T5ttcc with $m_{\tilde{g}} = 1.4$ TeV, $m_{\tilde{t}} = 320$ GeV and $m_{\tilde{\chi}^0_1} = 300$ GeV; T1tttt with $m_{\tilde{g}} = 1.4$ TeV and $m_{\tilde{\chi}^0_1} = 300$ GeV; and T2tt with $m_{\tilde{t}} = 850$ GeV and $m_{\tilde{\chi}^0_1} = 100$ GeV. The diagrams corresponding to these signal models are shown in Figure 24.

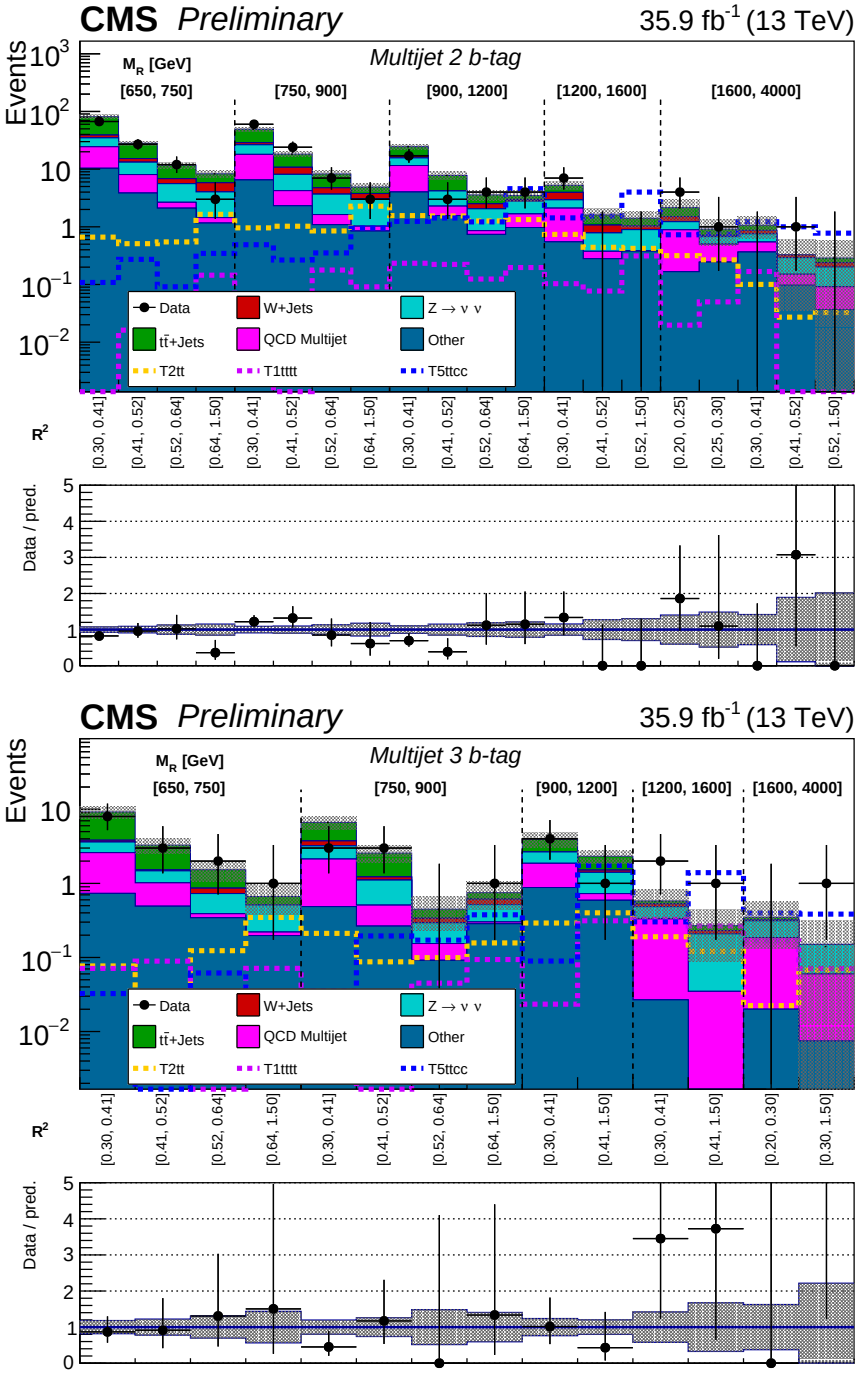

Figure 21: The M_R-R^2 distribution observed in data is shown along with the background prediction obtained for the Multijet event category in the 2 b-tag (top) and 3 b-tag (bottom) bins. The two-dimensional M_R-R^2 distribution is shown in a one dimensional representation, with each M_R bin marked by the dashed lines and labeled near the top, and each R^2 bin labeled below. The ratio of data to the background prediction is shown on the bottom inset, with the statistical uncertainty expressed through the data point error bars and the systematic uncertainty of the background prediction represented by the shaded region. Signal benchmarks shown are T5ttcc with $m_{\tilde{g}} = 1.4$ TeV, $m_{\tilde{t}} = 320$ GeV and $m_{\tilde{\chi}_1^0} = 300$ GeV; T1tttt with $m_{\tilde{g}} = 1.4$ TeV and $m_{\tilde{\chi}_1^0} = 300$ GeV; and T2tt with $m_{\tilde{t}} = 850$ GeV and $m_{\tilde{\chi}_1^0} = 100$ GeV. The diagrams corresponding to these signal models are shown in Figure 24.

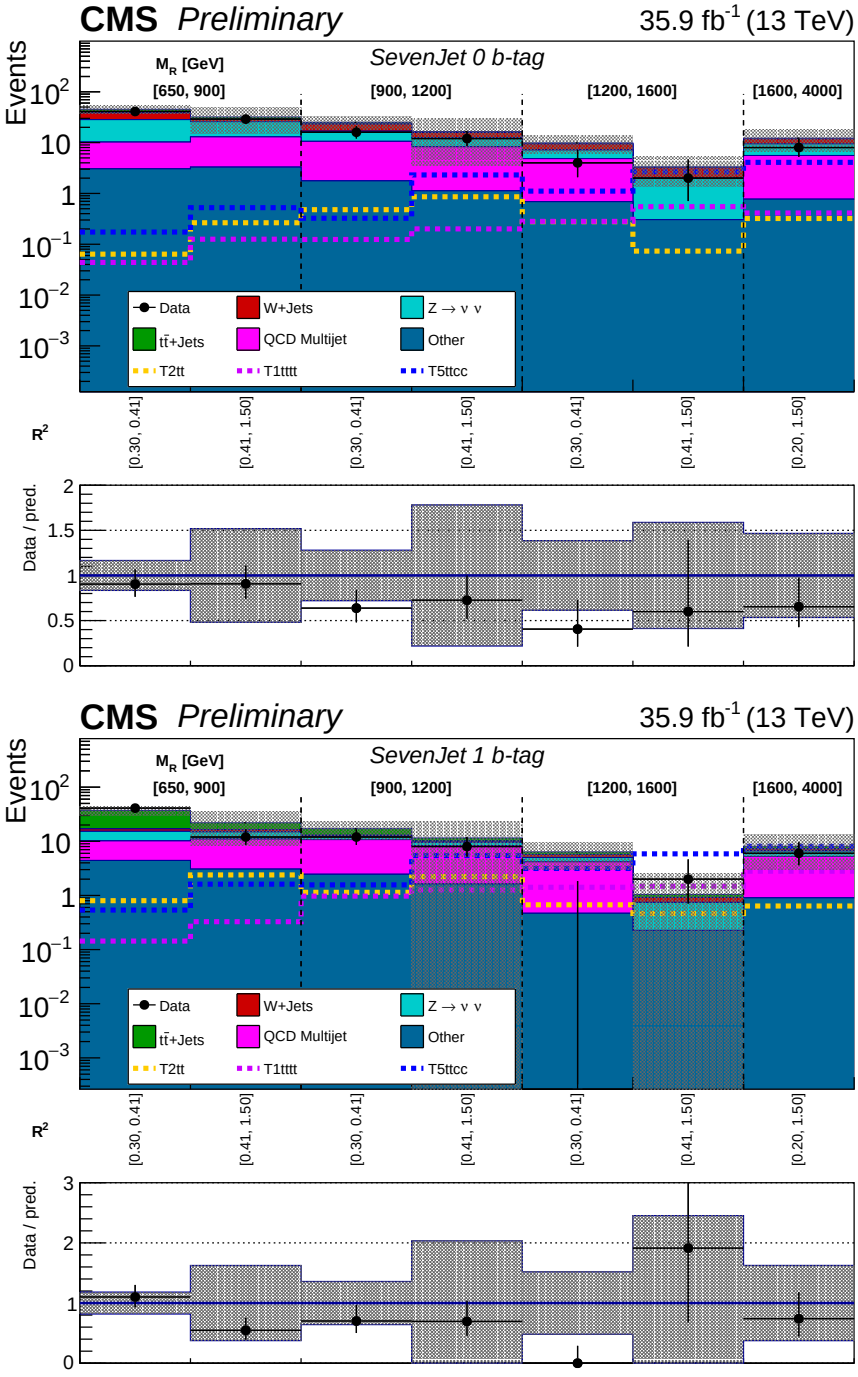

Figure 22: The M_R-R^2 distribution observed in data is shown along with the background prediction obtained for the Seven-jet event category in the 0 b-tag (top) and 1 b-tag (bottom) bins. The two-dimensional M_R-R^2 distribution is shown in a one dimensional representation, with each M_R bin marked by the dashed lines and labeled near the top, and each R^2 bin labeled below. The ratio of data to the background prediction is shown on the bottom inset, with the statistical uncertainty expressed through the data point error bars and the systematic uncertainty of the background prediction represented by the shaded region. Signal benchmarks shown are T5ttcc with $m_{\tilde{g}} = 1.4$ TeV, $m_{\tilde{t}} = 320$ GeV and $m_{\tilde{\chi}_1^0} = 300$ GeV; T1tttt with $m_{\tilde{g}} = 1.4$ TeV and $m_{\tilde{\chi}_1^0} = 300$ GeV; and T2tt with $m_{\tilde{t}} = 850$ GeV and $m_{\tilde{\chi}_1^0} = 100$ GeV. The diagrams corresponding to these signal models are shown in Figure 24.

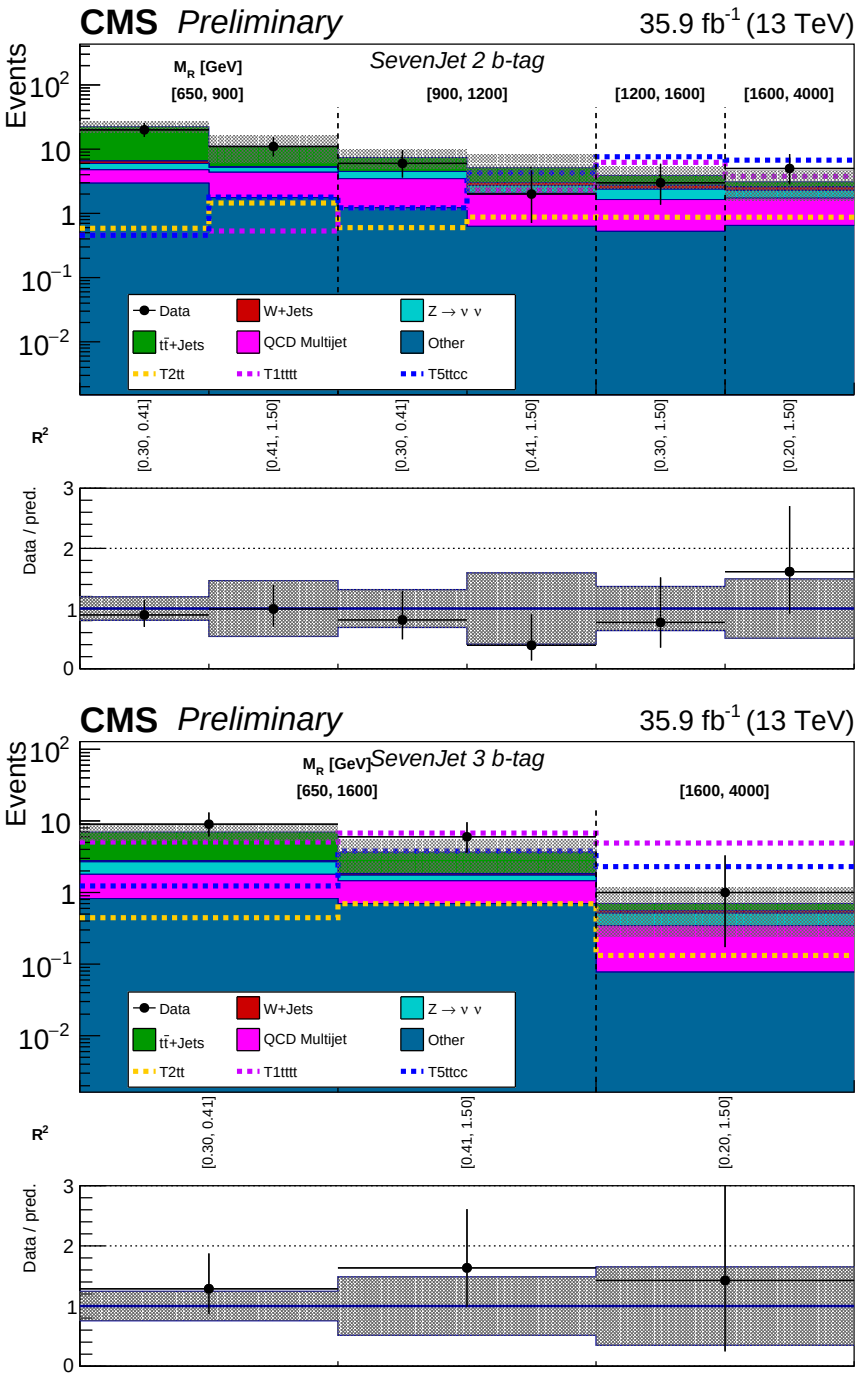

Figure 23: The M_R-R^2 distribution observed in data is shown along with the background prediction obtained for the Seven-jet event category in the 2 b-tag (top) and 3 b-tag (bottom) bins. The two-dimensional M_R-R^2 distribution is shown in a one dimensional representation, with each M_R bin marked by the dashed lines and labeled near the top, and each R^2 bin labeled below. The ratio of data to the background prediction is shown on the bottom inset, with the statistical uncertainty expressed through the data point error bars and the systematic uncertainty of the background prediction represented by the shaded region. Signal benchmarks shown are T5ttcc with $m_{\tilde{g}} = 1.4$ TeV, $m_{\tilde{t}} = 320$ GeV and $m_{\tilde{\chi}^0_1} = 300$ GeV; T1tttt with $m_{\tilde{g}} = 1.4$ TeV and $m_{\tilde{\chi}^0_1} = 300$ GeV; and T2tt with $m_{\tilde{t}} = 850$ GeV and $m_{\tilde{\chi}^0_1} = 100$ GeV. The diagrams corresponding to these signal models are shown in Figure 24.

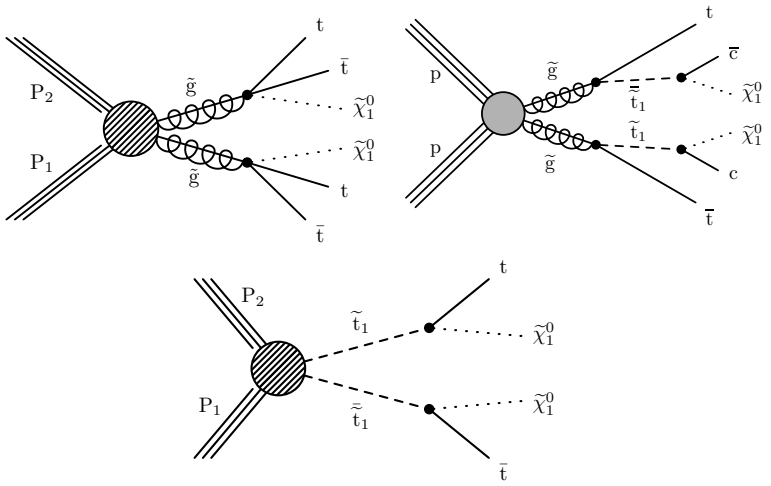

Figure 24: Diagrams for the simplified models considered in this analysis: (left) Gluino pair production decaying to two top quarks and the LSP, denoted T1tttt; (middle) Gluino pair production decaying to a top quark and a low mass top squark, which subsequently decays to a charm quark and the LSP, denoted T5ttcc; (right) Top squark pair production decaying to a top quark and the LSP, denoted T2tt.

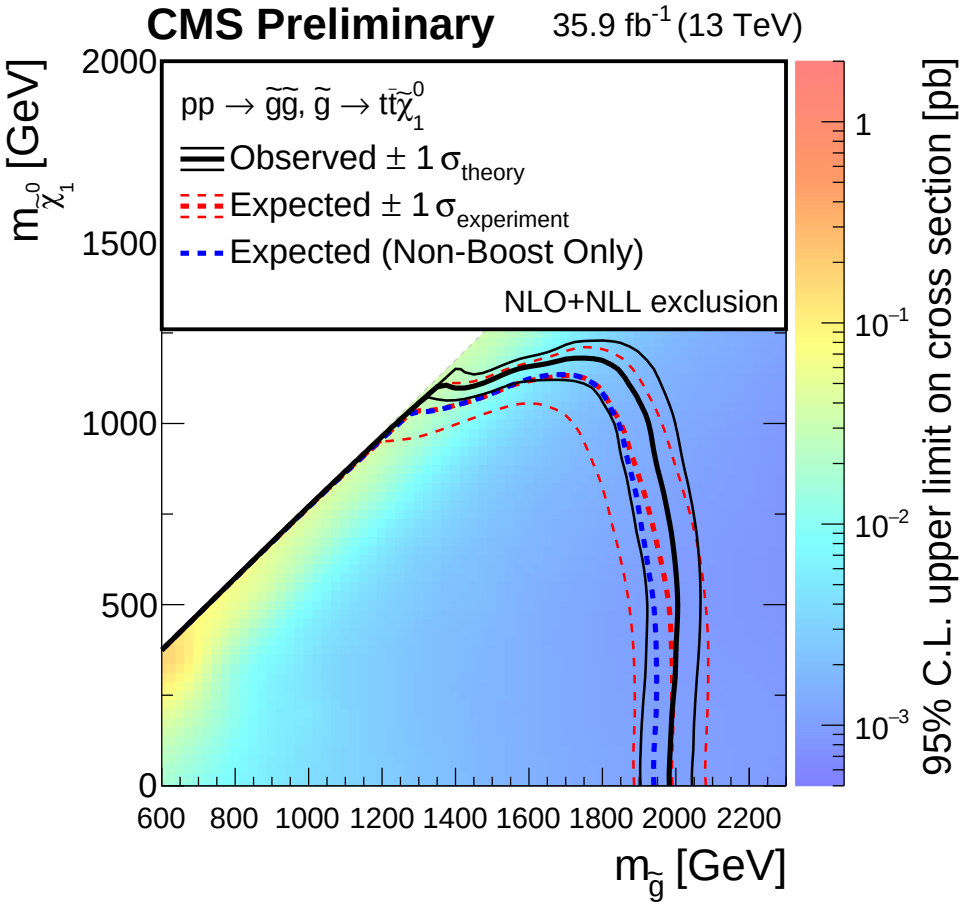

Figure 25: Expected and observed 95% upper limits on the production cross section for pair-produced gluinos decaying to top quarks. The blue dotted contour represents the expected 95% upper limits using data in the nonboosted categories only.

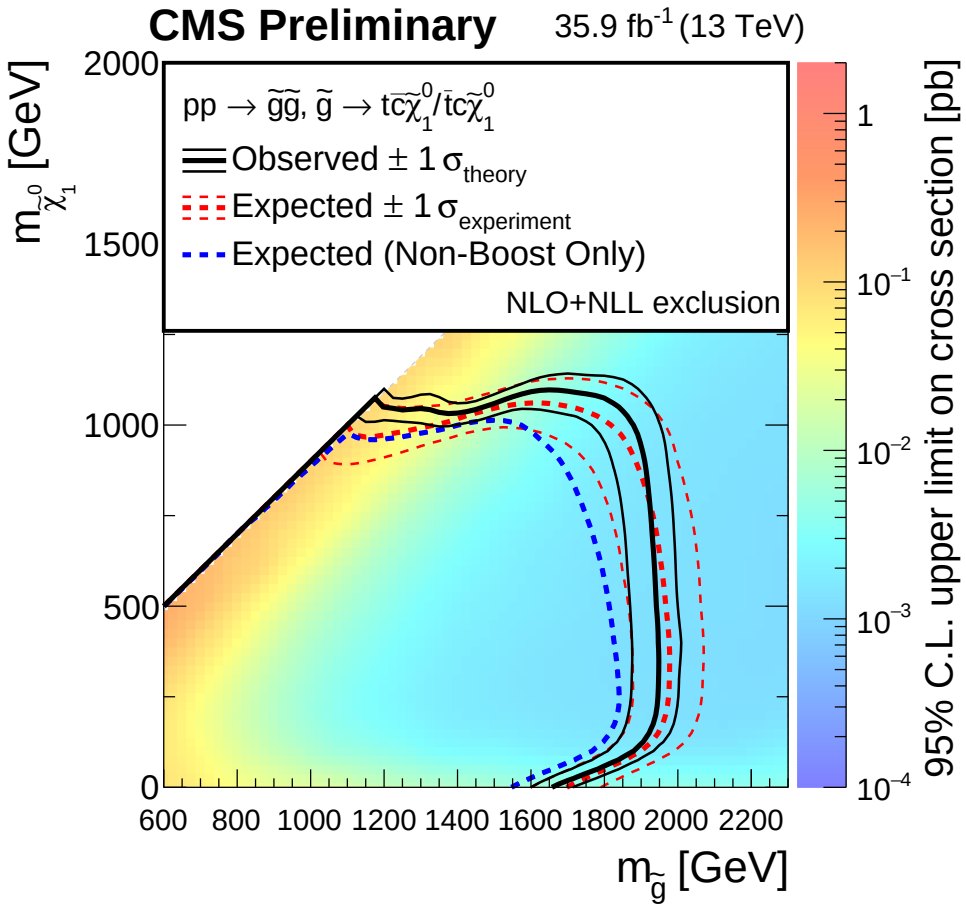

Figure 26: Expected and observed 95% upper limit on the production cross section for pair-produced gluinos decaying to a top and a charm quark. The blue dotted contour represents the expected 95% upper limits using data in the nonboosted categories only.

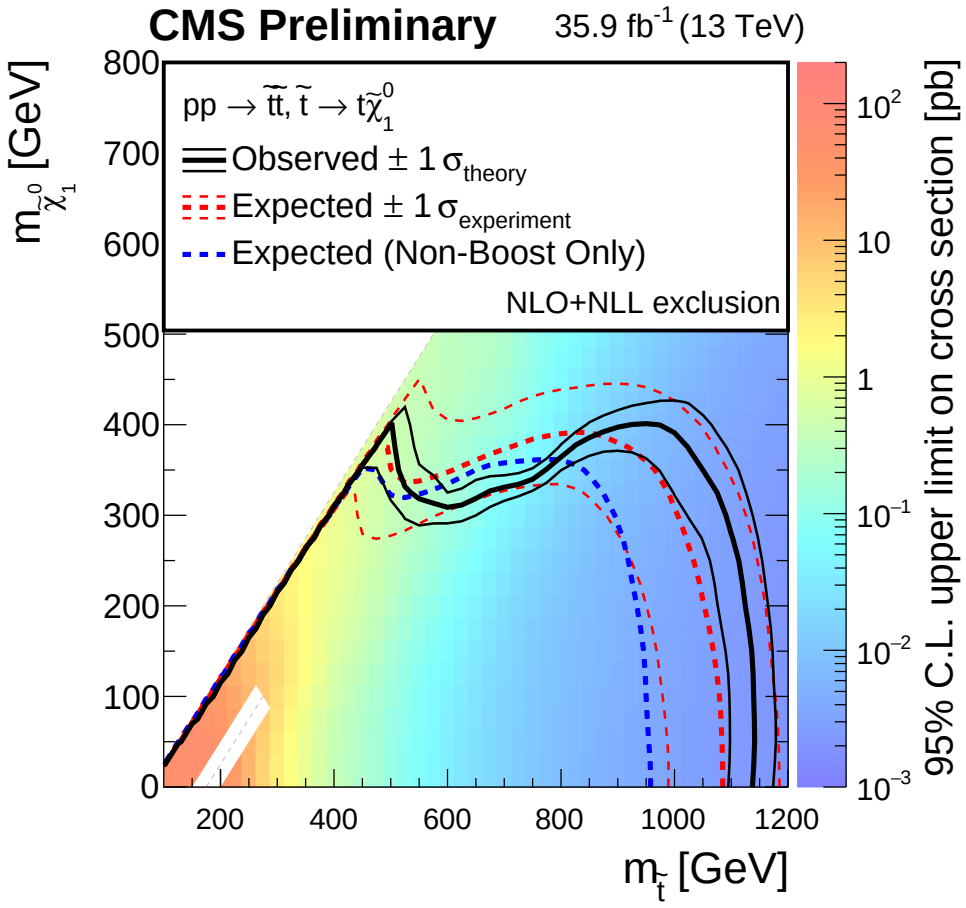

Figure 27: Expected and observed 95% upper limits on the production cross section for pair-produced squarks decaying to top quarks. The blue dotted contour represents the expected 95% upper limits using data in the nonboosted categories only. The white diagonal band corresponds to the region $|m_{\tilde{t}} - m_t - m_{\tilde{\chi}_1^0}| < 25\,\text{GeV}$, where the signal efficiency is a strong function of $m_{\tilde{t}} - m_{\tilde{\chi}_1^0}$, and as a result the precise determination of the cross section upper limit is uncertain because of the finite granularity of the available MC samples in this region of the $(m_{\tilde{t}}, m_{\tilde{\chi}_1^0})$ plane.

References

[1] CMS Collaboration, "Inclusive search for supersymmetry using razor variables in pp collisions at $\sqrt{s} = 13$ TeV", *Phys. Rev. D* **95** (2017) 012003, doi:10.1103/PhysRevD.95.012003, arXiv:1609.07658.

[2] CMS Collaboration, "Search for supersymmetry in pp collisions at $\sqrt{s} = 8$ TeV in final states with boosted W bosons and b jets using razor variables", *Phys. Rev.* **D93** (2016) 092009, doi:10.1103/PhysRevD.93.092009, arXiv:1602.02917.

[3] J. Wess and B. Zumino, "Supergauge transformations in four dimensions", *Nucl. Phys. B* **70** (1974) 39, doi:10.1016/0550-3213(74)90355-1.

[4] Y. A. Gol'fand and E. P. Likhtman, "Extension of the algebra of poincare group generators and violation of P invariance", *JETP Lett.* **13** (1971) 323.

[5] D. V. Volkov and V. P. Akulov, "Possible universal neutrino interaction", *JETP Lett.* **16** (1972) 438.

[6] A. H. Chamseddine, R. L. Arnowitt, and P. Nath, "Locally supersymmetric grand unification", *Phys. Rev. Lett.* **49** (1982) 970, doi:10.1103/PhysRevLett.49.970.

[7] G. L. Kane, C. F. Kolda, L. Roszkowski, and J. D. Wells, "Study of constrained minimal supersymmetry", *Phys. Rev. D* **49** (1994) 6173, doi:10.1103/PhysRevD.49.6173, arXiv:hep-ph/9312272.

[8] P. Fayet, "Supergauge invariant extension of the Higgs mechanism and a model for the electron and its neutrino", *Nucl. Phys. B* **90** (1975) 104, doi:10.1016/0550-3213(75)90636-7.

[9] R. Barbieri, S. Ferrara, and C. A. Savoy, "Gauge models with spontaneously broken local supersymmetry", *Phys. Lett. B* **119** (1982) 343, doi:10.1016/0370-2693(82)90685-2.

[10] L. J. Hall, J. D. Lykken, and S. Weinberg, "Supergravity as the messenger of supersymmetry breaking", *Phys. Rev. D* **27** (1983) 2359, doi:10.1103/PhysRevD.27.2359.

[11] P. Ramond, "Dual theory for free fermions", *Phys. Rev. D* **3** (1971) 2415, doi:10.1103/PhysRevD.3.2415.

[12] E. Witten, "Dynamical Breaking of Supersymmetry", *Nucl. Phys.* **B188** (1981) 513, doi:10.1016/0550-3213(81)90006-7.

[13] S. Dimopoulos and H. Georgi, "Softly Broken Supersymmetry and SU(5)", *Nucl. Phys.* **B193** (1981) 150, doi:10.1016/0550-3213(81)90522-8.

[14] M. Dine, W. Fischler, and M. Srednicki, "Supersymmetric Technicolor", *Nucl. Phys.* **B189** (1981) 575–593, doi:10.1016/0550-3213(81)90582-4.

[15] S. Dimopoulos and S. Raby, "Supercolor", *Nucl. Phys.* **B192** (1981) 353, doi:10.1016/0550-3213(81)90430-2.

[16] N. Sakai, "Naturalness in Supersymmetric Guts", *Z. Phys.* **C11** (1981) 153, doi:10.1007/BF01573998.

[17] R. K. Kaul and P. Majumdar, "Cancellation of Quadratically Divergent Mass Corrections in Globally Supersymmetric Spontaneously Broken Gauge Theories", *Nucl. Phys.* **B199** (1982) 36, doi:10.1016/0550-3213(82)90565-X.

[18] S. Dimopoulos, S. Raby, and F. Wilczek, "Supersymmetry and the Scale of Unification", *Phys. Rev.* **D24** (1981) 1681–1683, doi:10.1103/PhysRevD.24.1681.

[19] W. J. Marciano and G. Senjanovic, "Predictions of Supersymmetric Grand Unified Theories", *Phys. Rev.* **D25** (1982) 3092, doi:10.1103/PhysRevD.25.3092.

[20] M. B. Einhorn and D. R. T. Jones, "The Weak Mixing Angle and Unification Mass in Supersymmetric SU(5)", *Nucl. Phys.* **B196** (1982) 475, doi:10.1016/0550-3213(82)90502-8.

[21] L. E. Ibanez and G. G. Ross, "Low-Energy Predictions in Supersymmetric Grand Unified Theories", *Phys. Lett.* **B105** (1981) 439, doi:10.1016/0370-2693(81)91200-4.

[22] U. Amaldi, W. de Boer, and H. Furstenau, "Comparison of grand unified theories with electroweak and strong coupling constants measured at LEP", *Phys. Lett.* **B260** (1991) 447–455, doi:10.1016/0370-2693(91)91641-8.

[23] P. Langacker and N. Polonsky, "The Strong coupling, unification, and recent data", *Phys. Rev.* **D52** (1995) 3081–3086, doi:10.1103/PhysRevD.52.3081, arXiv:hep-ph/9503214.

[24] J. R. Ellis et al., "Supersymmetric Relics from the Big Bang", *Nucl. Phys.* **B238** (1984) 453–476, doi:10.1016/0550-3213(84)90461-9.

[25] G. Jungman, M. Kamionkowski, and K. Griest, "Supersymmetric dark matter", *Phys. Rept.* **267** (1996) 195–373, doi:10.1016/0370-1573(95)00058-5, arXiv:hep-ph/9506380.

[26] CMS Collaboration, "Search for natural and split supersymmetry in proton-proton collisions at $\sqrt{s} = 13$ TeV in final states with jets and missing transverse momentum", *JHEP* **05** (2018) 025, doi:10.1007/JHEP05(2018)025, arXiv:1802.02110.

[27] CMS Collaboration, "Search for top squark pair production in pp collisions at $\sqrt{s} = 13$ TeV using single lepton events", *JHEP* **10** (2017) 019, doi:10.1007/JHEP10(2017)019, arXiv:1706.04402.

[28] CMS Collaboration, "Search for new phenomena with the M_{T2} variable in the all-hadronic final state produced in proton-proton collisions at $\sqrt{s} = 13$ TeV", *Eur. Phys. J.* **C77** (2017) 710, doi:10.1140/epjc/s10052-017-5267-x, arXiv:1705.04650.

[29] CMS Collaboration, "Search for Supersymmetry in pp Collisions at $\sqrt{s} = 13$ TeV in the Single-Lepton Final State Using the Sum of Masses of Large-Radius Jets", *Phys. Rev. Lett.* **119** (2017) 151802, doi:10.1103/PhysRevLett.119.151802, arXiv:1705.04673.

[30] CMS Collaboration, "Search for supersymmetry in multijet events with missing transverse momentum in proton-proton collisions at 13 TeV", *Phys. Rev.* **D96** (2017) 032003, doi:10.1103/PhysRevD.96.032003, arXiv:1704.07781.

[31] CMS Collaboration, "Search for physics beyond the standard model in events with two leptons of same sign, missing transverse momentum, and jets in proton-proton collisions at $\sqrt{s} = 13$ TeV", *Eur. Phys. J.* **C77** (2017) 578, doi:10.1140/epjc/s10052-017-5079-z, arXiv:1704.07323.

[32] CMS Collaboration, "Search for supersymmetry in the all-hadronic final state using top quark tagging in pp collisions at $\sqrt{s} = 13$ TeV", *Phys. Rev.* **D96** (2017) 012004, doi:10.1103/PhysRevD.96.012004, arXiv:1701.01954.

[33] CMS Collaboration, "Searches for pair production of third-generation squarks in $\sqrt{s} = 13$ TeV pp collisions", *Eur. Phys. J.* **C77** (2017) 327, doi:10.1140/epjc/s10052-017-4853-2, arXiv:1612.03877.

[34] ATLAS Collaboration, "Search for a scalar partner of the top quark in the jets plus missing transverse momentum final state at $\sqrt{s} = 13$ TeV with the ATLAS detector", *JHEP* **12** (2017) 085, doi:10.1007/JHEP12(2017)085, arXiv:1709.04183.

[35] ATLAS Collaboration, "Search for supersymmetry in events with b-tagged jets and missing transverse momentum in pp collisions at $\sqrt{s} = 13$ TeV with the ATLAS detector", *JHEP* **11** (2017) 195, doi:10.1007/JHEP11(2017)195, arXiv:1708.09266.

[36] ATLAS Collaboration, "Search for squarks and gluinos in events with an isolated lepton, jets, and missing transverse momentum at $\sqrt{s} = 13$ TeV with the ATLAS detector", *Phys. Rev.* **D96** (2017) 112010, doi:10.1103/PhysRevD.96.112010, arXiv:1708.08232.

[37] ATLAS Collaboration, "Search for direct top squark pair production in final states with two leptons in $\sqrt{s} = 13$ TeV pp collisions with the ATLAS detector", *Eur. Phys. J.* **C77** (2017) 898, doi:10.1140/epjc/s10052-017-5445-x, arXiv:1708.03247.

[38] ATLAS Collaboration, "Search for new phenomena with large jet multiplicities and missing transverse momentum using large-radius jets and flavour-tagging at ATLAS in 13 TeV pp collisions", *JHEP* **12** (2017) 034, doi:10.1007/JHEP12(2017)034, arXiv:1708.02794.

[39] ATLAS Collaboration, "Search for supersymmetry in final states with two same-sign or three leptons and jets using 36 fb^{-1} of $\sqrt{s} = 13$ TeV pp collision data with the ATLAS detector", *JHEP* **09** (2017) 084, doi:10.1007/JHEP09(2017)084, arXiv:1706.03731.

[40] ATLAS Collaboration, "Search for new phenomena in a lepton plus high jet multiplicity final state with the ATLAS experiment using $\sqrt{s} = 13$ TeV proton-proton collision data", *JHEP* **09** (2017) 088, doi:10.1007/JHEP09(2017)088, arXiv:1704.08493.

[41] CMS Collaboration, "The CMS experiment at the CERN LHC", *JINST* **3** (2008) S08004, doi:10.1088/1748-0221/3/08/S08004.

[42] CMS Collaboration, "Particle-flow reconstruction and global event description with the CMS detector", *JINST* **12** (2017) P10003, doi:10.1088/1748-0221/12/10/P10003, arXiv:1706.04965.

[43] M. Cacciari, G. P. Salam, and G. Soyez, "The anti-k_t jet clustering algorithm", *JHEP* **04** (2008) 063, doi:10.1088/1126-6708/2008/04/063, arXiv:0802.1189.

[44] M. Cacciari, G. P. Salam, and G. Soyez, "FastJet user manual", *Eur. Phys. J. C* **72** (2012) 1896, doi:10.1140/epjc/s10052-012-1896-2, arXiv:1111.6097.

[45] CMS Collaboration, "Identification of heavy-flavour jets with the CMS detector in pp collisions at 13 TeV", *JINST* **13** (2018) P05011, doi:10.1088/1748-0221/13/05/P05011, arXiv:1712.07158.

[46] J. Thaler and K. Van Tilburg, "Identifying boosted objects with N-subjettiness", *JHEP* **03** (2011) 015, doi:10.1007/JHEP03(2011)015, arXiv:1011.2268.

[47] A. J. Larkoski, S. Marzani, G. Soyez, and J. Thaler, "Soft Drop", *JHEP* **05** (2014) 146, doi:10.1007/JHEP05(2014)146, arXiv:1402.2657.

[48] CMS Collaboration, "Performance of Electron Reconstruction and Selection with the CMS Detector in Proton-Proton Collisions at 8 TeV", *JINST* **10** (2015) P06005, doi:10.1088/1748-0221/10/06/P06005, arXiv:1502.02701.

[49] CMS Collaboration, "Performance of CMS muon reconstruction in pp collision events at $\sqrt{s} = 7$ TeV", *JINST* **7** (2012) P10002, doi:10.1088/1748-0221/7/10/P10002, arXiv:1206.4071.

[50] CMS Collaboration, "Reconstruction and identification of τ lepton decays to hadrons and ν_τ at CMS", *JINST* **11** (2016) P01019, doi:10.1088/1748-0221/11/01/P01019, arXiv:1510.07488.

[51] CMS Collaboration, "Performance of photon reconstruction and identification with the CMS detector in proton-proton collisions at $\sqrt{s} = 8$ TeV", *JINST* **10** (2015) P08010, doi:10.1088/1748-0221/10/08/P08010, arXiv:1502.02702.

[52] J. Alwall et al., "MadGraph5: going beyond", *JHEP* **06** (2011) 128, doi:10.1007/JHEP06(2011)128, arXiv:1106.0522.

[53] T. Sjöstrand, S. Mrenna, and P. Z. Skands, "A Brief Introduction to PYTHIA 8.1", *Comput. Phys. Commun.* **178** (2008) 852–867, doi:10.1016/j.cpc.2008.01.036, arXiv:0710.3820.

[54] T. Sjöstrand et al., "An Introduction to PYTHIA 8.2", *Comput. Phys. Commun.* **191** (2015) 159–177, doi:10.1016/j.cpc.2015.01.024, arXiv:1410.3012.

[55] S. Hoeche et al., "Matching parton showers and matrix elements", in *HERA and the LHC: A Workshop on the implications of HERA for LHC physics: Proceedings Part A*, pp. 288–289. 2005. arXiv:hep-ph/0602031. doi:10.5170/CERN-2005-014.288.

[56] J. Alwall et al., "Comparative study of various algorithms for the merging of parton showers and matrix elements in hadronic collisions", *Eur. Phys. J.* **C53** (2008) 473–500, doi:10.1140/epjc/s10052-007-0490-5, arXiv:0706.2569.

[57] J. Alwall et al., "The automated computation of tree-level and next-to-leading order differential cross sections, and their matching to parton shower simulations", *JHEP* **07** (2014) 079, doi:10.1007/JHEP07(2014)079, arXiv:1405.0301.

[58] S. Frixione, P. Nason, and G. Ridolfi, "A Positive-weight next-to-leading-order Monte Carlo for heavy flavour hadroproduction", *JHEP* **09** (2007) 126, doi:10.1088/1126-6708/2007/09/126, arXiv:0707.3088.

[59] S. Alioli, P. Nason, C. Oleari, and E. Re, "NLO single-top production matched with shower in POWHEG: s- and t-channel contributions", *JHEP* **09** (2009) 111, doi:10.1007/JHEP02(2010)011, 10.1088/1126-6708/2009/09/111, arXiv:0907.4076. [Erratum: JHEP02,011(2010)].

[60] E. Re, "Single-top Wt-channel production matched with parton showers using the POWHEG method", *Eur. Phys. J.* **C71** (2011) 1547, doi:10.1140/epjc/s10052-011-1547-z, arXiv:1009.2450.

[61] S. Agostinelli et al., "Geant4 - a simulation toolkit", *Nucl. Instrum. Meth. A* **506** (2003) 250 – 303, doi:http://dx.doi.org/10.1016/S0168-9002(03)01368-8.

[62] CMS Collaboration, "The fast simulation of the CMS detector at LHC", *J. Phys.: Conf. Ser.* **331** (2011) 032049, doi:10.1088/1742-6596/331/3/032049.

[63] W. Beenakker, R. Höpker, M. Spira, and P. M. Zerwas, "Squark and gluino production at hadron colliders", *Nucl. Phys. B* **492** (1997) 51, doi:10.1016/S0550-3213(97)80027-2, arXiv:hep-ph/9610490.

[64] A. Kulesza and L. Motyka, "Threshold resummation for squark-antisquark and gluino-pair production at the LHC", *Phys. Rev. Lett.* **102** (2009) 111802, doi:10.1103/PhysRevLett.102.111802, arXiv:0807.2405.

[65] A. Kulesza and L. Motyka, "Soft gluon resummation for the production of gluino-gluino and squark-antisquark pairs at the LHC", *Phys. Rev. D* **80** (2009) 095004, doi:10.1103/PhysRevD.80.095004, arXiv:0905.4749.

[66] W. Beenakker et al., "Soft-gluon resummation for squark and gluino hadroproduction", *JHEP* **12** (2009) 041, doi:10.1088/1126-6708/2009/12/041, arXiv:0909.4418.

[67] W. Beenakker et al., "Squark and gluino hadroproduction", *Int. J. Mod. Phys. A* **26** (2011) 2637, doi:10.1142/S0217751X11053560, arXiv:1105.1110.

[68] C. Borschensky et al., "Squark and gluino production cross sections in pp collisions at $\sqrt{s} = 13$, 14, 33 and 100 TeV", *Eur. Phys. J.* **C74** (2014) 3174, doi:10.1140/epjc/s10052-014-3174-y, arXiv:1407.5066.

[69] M. Kramer et al., "Supersymmetry production cross sections in pp collisions at $\sqrt{s} = 7$ TeV", arXiv:1206.2892.

[70] CMS Collaboration, "Inclusive search for squarks and gluinos in pp collisions at $\sqrt{s} = 7$ TeV", *Phys. Rev. D* **85** (2012) 012004, doi:10.1103/PhysRevD.85.012004, arXiv:1107.1279.

[71] CMS Collaboration, "Missing transverse energy performance of the CMS detector", *JINST* **6** (2011) P09001, doi:10.1088/1748-0221/6/09/P09001, arXiv:1106.5048.

[72] CMS Collaboration, "Performance of the CMS missing transverse momentum reconstruction in pp data at $\sqrt{s} = 8$ TeV", *JINST* **10** (2015) P02006, doi:10.1088/1748-0221/10/02/P02006, arXiv:1411.0511.

[73] ATLAS and CMS Collaborations, "Procedure for the LHC Higgs boson search combination in summer 2011", CMS NOTE/ATL-PHYS-PUB ATL-PHYS-PUB-2011-011, CMS-NOTE-2011-005, CERN, 2011.

[74] CMS Collaboration, "Search for supersymmetry in proton-proton collisions at 13 TeV using identified top quarks", *Phys. Rev.* **D97** (2018) 012007, doi:10.1103/PhysRevD.97.012007, arXiv:1710.11188.